David Simões de Melo

Bachelor Degree in Engineering Sciences

Optical Design of a Retinal Image Acquisition Device for Mobile Diabetic Retinopathy Assessment

Dissertation submitted in partial fulfillment
of the requirements for the degree of

Master of Science in
Biomedical Engineering

Adviser: Pedro Manuel Cardoso Vieira, Professor,
NOVA University of Lisbon

Co-adviser: Filipe Soares, PhD, Fraunhofer Portugal AICOS

Examination Committee

Chairperson: Carla Quintão, Professor, NOVA University of Lisbon
Members: Paulo Ribeiro, Professor, NOVA University of Lisbon
Pedro Vieira, Professor, NOVA University of Lisbon

FACULDADE DE
CIÊNCIAS E TECNOLOGIA
UNIVERSIDADE NOVA DE LISBOA

September, 2017

Optical Design of a Retinal Image Acquisition Device for Mobile Diabetic Retinopathy Assessment

This document was created using the (pdf)LaTeX processor, based in the "novathesis" template[1], developed at the Dep. Informática of FCT-NOVA [2].
[1] https://github.com/joaomlourenco/novathesis [2] http://www.di.fct.unl.pt

Acknowledgements

The realization of this master thesis have counted with the support of the Fraunhofer Portugal AICOS institution, giving me all the tools needed for the development of a continuously challenging work. More specifically, I want to thank all the persons responsible for the ScreeningEFSOptics that guide me through all the company procedures, individually João Costa, for his continuous availability and important inputs week after week and Filipe Soares for his always helpful hints.

I would also like to thank the Lisbon office team. Without their continuous good mood and inputs, the realization of this thesis wouldn't have been so much cheerful.

I would also like to thank my Adviser Professor Pedro Vieira from FCT NOVA for making me always look for the positive side of any problem that appeared, for providing with all the necessary inputs and for steering me in the right direction to overcome any of the challenges I was put to proof.

For my family, high school and college friends, I want to thank them for granting me with their beneficial company, availability and for their valorous inputs during all the academic tests I was put up to.

Finally, I must express my very profound gratitude to my parents for providing me with unfailing support and continuous encouragement throughout my years of study and through the process of researching and writing this thesis. This accomplishment, as all the others I've ever achieved would not have been possible without such extraordinary role models to follow.

Thank you all for the encouragement!

Abstract

Diabetes mellitus is a condition that lead to various systemic alterations. These changes, taking place in the blood vessels cause a progressive capillary occlusion and, in the posterior eye region, provoke leakages from the vessels to the retina leading to a disease called diabetic retinopathy. This pathology ultimately can lead to complete vision loss, which is an aspect that emphasizes the relevance of the work developed in this thesis.

The initial progression is asymptomatic, so only in advanced and frequently irreversible stages, the patient becomes aware of the disease. For this reason, a regular follow-up accomplished by eye fundus examination should be performed. Even though, for logistic motivations (lack of equipment, absence of ophthalmology specialists...) the progression-study and diagnose of the disease is often neglected.

To encourage high coverage screening, a compact optical system was designed for a handheld and smartphone-based fundus camera prototype. The key features for the optical system are the low-cost achieved through a simple lens system and a mobile and non-mydriatic acquisition of fundus images with high field-of-view, by a smartphone camera.

The simplicity of the optical system was accomplished by a three lens system setup. The results reveal a system with only a few aberrations in the periphery but with a good resolution at the center of a 41° field-of-view.

Besides the optical system, a mechanical prototype was designed with the purpose of being 3D printed and easily portable.

Also, a light hazard testing procedure was established and applied on a previously developed prototype.

In the future, the implementation of the optical system in the prototype is intended, in order to confirm the applicability of the design in diminishing the burden of screening actions and consequently, empower the early treatment of the pathology.

Keywords: Diabetic Retinopathy; Fundus Camera; Optical System Design; Mechanical Prototyping; Light Hazard Measurement; Pupil Alignment

Resumo

A diabetes mellitus é uma condição que leva a várias alterações sistêmicas. Essas alterações, ocorrendo nos vasos sanguíneos, causam uma oclusão capilar progressiva que, na região posterior do olho, leva a uma doença chamada retinopatia diabética. Esta patologia, em última instância, pode levar a uma perda completa da visão, o que é um aspeto que enfatiza a relevância do trabalho desenvolvido durante esta tese.

A progressão inicial é assintomática, portanto, apenas em estágios avançados e frequentemente irreversíveis, o paciente toma conhecimento da doença. Por este motivo, um acompanhamento regular com realização de exame do fundo ocular deve ser realizado. No entanto, por várias motivações (falta de equipamento, ausência de oftalmologistas...), o estudo da progressão e o diagnóstico da doença são muitas vezes negligenciados.

Para incentivar o rastreio de alta cobertura, um sistema ótico compacto foi projetado para um protótipo de um retinógrafo portátil acoplado a um smartphone. As características-chave do sistema ótico são o baixo custo alcançado através de um sistema de lentes simples e a aquisição móvel e não-midriática de imagens do fundo com alto campo de visão, através da câmara de um smartphone.

A simplicidade do sistema ótico foi conseguida através duma configuração de três lentes. Os resultados revelam um sistema com uma boa resolução central e com 41° de campo de visão na retina.

Para além do sistema ótico, foi projetado um protótipo mecânico com o objetivo de ser impresso em 3D.

Um plano de testes de perigo ocular foi também estabelecido e aplicado num protótipo previamente desenvolvido.

No futuro, pretende-se a implementação do sistema ótico no protótipo, com o objetivo de confirmar a aplicabilidade do projeto na diminuição do peso das ações de rastreio e, consequentemente, possibilitar o tratamento precoce da doença.

Palavras-chave: Retinopatia Diabética; Retinógrafo; Desenho de Sistemas Óticos; Prototipagem Mecânica; Medições de Perigo Ocular; Alinhamento da Pupila.

Contents

List of Figures

List of Tables

Acronyms

BRB	Blood-Retinal Barrier.
DR	Diabetic Retinopathy.
FOV	Field-of-View.
LED	Light-Emitting-Diode.
NIR	Near Infra-Red.
NPDR	Non-proliferative Diabetic Retinopathy.
OCT	Optical Coherence Tomography.
PCX	Plano-Convex.
PDR	Proliferative Diabetic Retinopathy.
PWM	Pulse-Width Modulation.
VEGF	Vascular Endothelial Growth Factor.

Chapter 1

Introduction

In this thesis, a fundus camera prototype is designed in order to help directly in the diagnose of several ophthalmologic pathologies, mainly Diabetic Retinopathy.

Before the beginning of this work, a prototype had already been developed by Fraunhofer. The main problems present in this prototype were the amount of dispersion and the existence of undesired reflections, caused by the absence of stops and by the inner surface of the prototype reflectivity (not completely light absorbent), making it harder to acquire well-focused images. The impossibility of a continuous distance adjustment between components were other problems in this prototype. The conjunction of all these factors compromises the accuracy of the exam, making any possible medical deduction questionable, hardly allowing an indubitable diagnose. To overcome this, a new optical system as well as a 3D-printed prototype were designed.

For the design of the optical system, several lenses systems were simulated as presented in chapter 4, always considering a coherent relationship between the quality and the cost of the components. The key features for the compact optical system are the mobile and non-mydriatic acquisition of fundus images by a smartphone camera, with a 40° Field-of-View (FOV).

Light Hazard Measurements on a previously developed prototype were also performed, so safety issues concerning tests in healthcare institutions can be overcome.

1.1 Context and Motivation

Diabetes mellitus condition affects about 415 million of persons world-wide, of those 193 million are not diagnosed, and eventually unaware of its existence [1]. The Diabetic Retinopathy is a disease, caused by this condition, that affects 76% of the diabetic patients for longer than 20 years [2], being the leading cause of blindness in adults with working

age [3].

The asymptomatic profile of the initial progression of DR and the high effectiveness of early treatment have motivated the implementation of extensive screening programs covering the diabetic population, in which images of the patient retinas are acquired and subsequently analyzed by an expert. However, this requires the use of relatively expensive and cumbersome equipment to acquire the retinal images as well as a time-consuming analysis of those images by ophthalmologists. The prototype EyeFundusScope, currently under investigation by Fraunhofer Portugal AICOS, aims to address these two issues by researching on a self-contained solution comprising automated diabetic retinopathy detection with a low cost optical attachment to a smartphone for retinal image acquisition. The major goal is to improve patient access to early treatment and decrease the burden of screening actions on healthcare systems all over the world.

With this work, improvements in the telemedicine field are also expected, by the acquisition and free-sharing of fundus photographies between nonspecialist and specialist personnel, increasing the comfort and the assiduity of the eye fundus examination.

1.2 Objectives

The 3 principal objectives targeted during this thesis were:

- Design of a compact optical system for fundus photography with no need of pupil dilation, ensuring 40º field-of-view with a uniform illumination in all the desired area, comprising several pupil alignments;
- Design of a 3D-printed mechanical prototype for support of the optical system, facilitating transportation and handheld screening;
- Light Hazard measurement on a previously developed fundus camera prototype.

The design of a compact, small optical system urges since there is the need of an handheld smartphone based device for easy transportation and to be used in under-developed countries. The requirements on the field of view and the no need of pupil dilation are essential for an easy acquisition, easily performed by individuals with no experience on ophthalmology or orthoptics enhancing the role of the telemedicine in the global healthcare. Are comprised the acquisition of ocular fundus photographs, its share with the doctor, the medical appreciation and finally, the communication of the diagnose to the patient. In the optical system the implementation of internal fixation points will also be addressed. The existence of internal fixation points will also be a very important feature for the prototype. By giving the patient a target to be staring on, the eye movements are prevented, furthering the idea of a non-specialized examiner.

An ergonomic 3D-printed mechanical prototype adjusted for the lens system developed will be designed in order to allow the transportation and an easier dissemination of the prototype world-wide.

The light hazard measurement on the previous prototype was also accessed, regarding two different ISO norms, ISO 15004-2[4] for Light Hazard Protection on Ophthalmic Instruments and ISO 10940[5] for fundus cameras. For each LED, both the power emitted and the spectrum were obtained as well as the power emitted during the acquisition of the image (flash of the smartphone camera).

1.3 Overview

This dissertation is divided in 8 chapters. In this one, are explained the initial problem and the objectives expected to be achieved by end of this thesis.

In chapter 2, Diabetic Retinopathy, the disease whose diagnose and morbidity is intended to be diminished by the work developed during this thesis, is explained, as well as the fundamental characteristics of a fundus camera, the instrument to be designed.

In chapter 3, there is a guide for the optical system design software, BEAM IV, as well as an explanation of several optical principles, helpful in the achievement of an accurate optical system.

Chapter 4 presents the different optical simulations performed, the human eye, the optical system in the previous prototype, the developed optical system with an explanation on the adjustments needed for patients with different refractive errors and the design of internal fixation points.

In chapter 5, the mechanical prototype designed for the casing of the optical system is presented along with the specifications required.

In chapter 6, a description of the Light Hazard Measurements along with a ISO Norms compliance test is presented.

In chapter 7, the Imaging path, designed in BEAM IV, practical tests performed in an optics laboratory are described. The Imaging path for refractive errors tests are also addressed.

At last, in chapter 8, a conclusion of this work is presented along with some topics important for the future implementation of the system designed during this thesis.

Chapter 2

Diabetic Retinopathy

Diabetic Retinopathy is a microvascular consequence of diabetes, characterized by the loss of pericytes and by a progressive capillary occlusion that occurs mostly without symptoms. The capillary occlusion can lead to retinal ischemia and to the breakdown of the blood-retinal-barrier[6]. As the Diabetic Retinopathy (DR) advances, the risk of blindness increases. In addition, patients with DR have higher chances of contracting coronary heart disease, stroke, diabetic nephropathy, or amputations [7]. The major risk factors are the existence of diabetes mellitus condition, poor glycemic control and hypertension [8, 9].

In addition to a strict systemic control of glycemic, lipid, cholesterol and blood pressure levels, routine ophthalmologic examination has a vital role in the early identification of diabetic retinopathy, facilitating the treatment of the disease in a initial stage[10, 11].

The DR is commonly divided in two different stages: Non-proliferative Diabetic Retinopathy (NPDR) and Proliferative Diabetic Retinopathy (PDR). The first is characterized by abnormalities in the blood vessels, materialized in the leakage of substances from the lumen of the vessels to the retinal epithelium. The leakages may be the blood itself leading to microaneurysms and intraretinal hemorrhages, and lipids leading to hard and soft exudates [11–13]. It is classified according to its severity in [11–13] :

- Mild- at least one microaneurysm;
- Moderate - presence of blood hemorrhages;
- Severe (4-2-1) - more than 20 hemorrhages in **4 quadrants**, vessel distensions in **2 quadrants** or intrarretinal microvascular abnormalities in **1 of the quadrants**.

The Proliferative stage is characterized by the creation of new blood vessels surrounding occluded regions (neovascularization) [11, 14]. The new blood vessels, being more fragile

than the previous ones, increase the risk of bleeding and do not solve retinal ischemia [13]. In this stage there is also the formation of fibrous tissue that while contracting can provoke retinal detachment[15].

The DR is a disease that ultimately can lead to complete vision loss (Figure 2.1) and its high morbidity is statistically proven, affecting 76% of the diabetic patients for longer than 20 years [2], being the leading cause of blindness in adults with working age [3].

a Vision showing no significant visual deficiencies. b Possible vision of a person with Diabetic Retinopathy.

Figure 2.1: Visual differences between an ophthalmological healthy person and a person with Diabetic Retinopathy. Both Images were obtained in a presentation supplied by Fraunhofer Portugal AICOS.

2.1 Pathology Progression

In the DR, mainly due to the exaggerated glucose level in the blood, several changes in the blood vessels occur. These changes consist in the thickening of the walls, reduction of the gauge, consistency, elasticity and permeability alterations, which lead to the symptoms progression as described in the following subsections [14, 16].

2.1.1 Non-Profilerative Diabetic Retinopathy

- Microaneurysm (Figure 2.2) :

  Are presented as small red dots with a well-defined shape [11]. Characteristics of an initial stage of the disease, its size(25 to 125 micrometers) [17], makes a rather high resolution, a requirement for every early-diagnostic device [13].

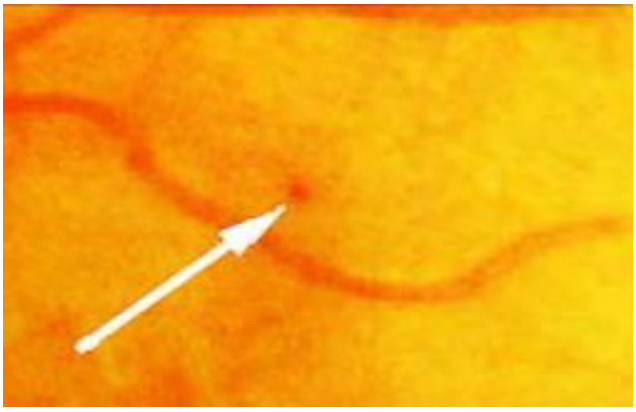

Figure 2.2: Image of a microaneurysm [12].

- Intrarretinal Hemorrhages (Figure 2.3):

  Caused by capillary rupture [12]. Can present a rounded shape, as microaneurysms, or have an undefined shape [13].

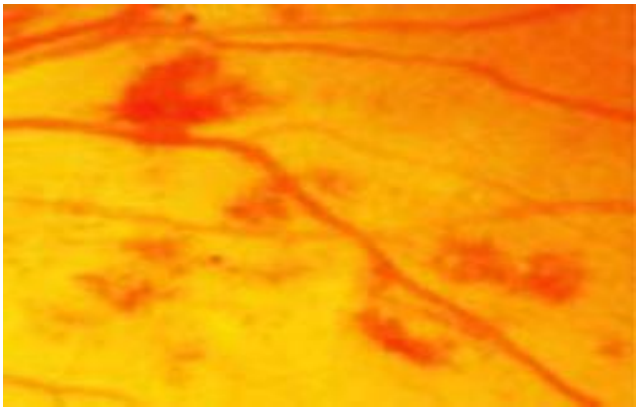

Figure 2.3: Image of an intrarretinal hemorrhage [12].

- Exudates (Figure 2.4):

Consist in the deposition of big chains of lipids or peptides, leaked from the blood vessels, on the retina. Usually, are yellow and can be grouped, as can be seen in Figure 2.4 [12, 13].

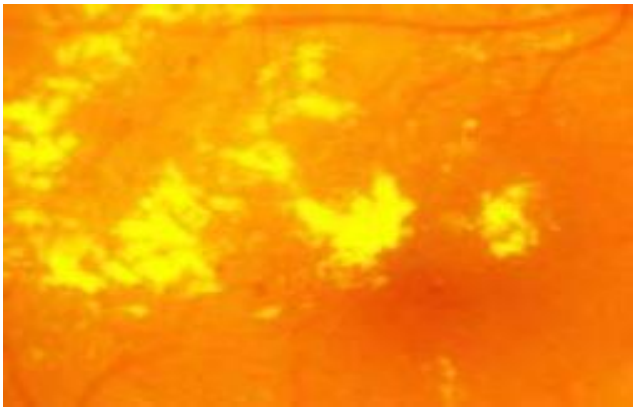

Figure 2.4: Image of an exsudate [12].

- Diabetic Macular Edema:

  Macular Edema is characterized by an increment on the thickness of the macula caused by the breakage of the Blood-Retinal Barrier (BRB), provoking the leakage of liquid from the lumen of the vessels to the retinal epithelium [18]. May not be seen in fundus photographs, although a notorious presence of exudates may indicate this complication. Is the main cause of blindness in patients with type 2 diabetes [13].

2.1.2 Profilerative Diabetic Retinopathy

- Neovascularization (Figure 2.5):

  New vessels are formed surrounding occluded regions as an attempt to restore the blood perfusion. The new blood vessels don't provide enough blood and are much more fragile, not solving ischemia and increasing the risk of hemorrhages in retinal epithelium [19]. This hemorrhages can lead to floaters (Figure 2.1b) and in some cases, blindness.

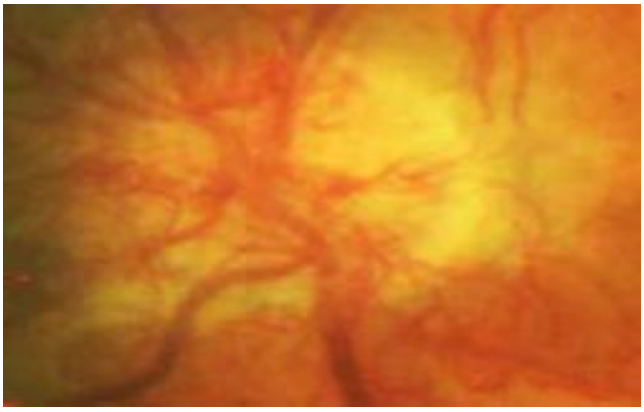

Figure 2.5: Neovascularization derived vessels covering the Optical Disk [12].

- Fibrous Tissue Formation

  During this stage of DR the new vessels become bigger and the formation of fibrous tissue takes place [19].

- Retinal Detachment (Figure 2.6)

  When the fibrous tissue contracts, the retina can be tractionally detached from the fundus, leading to serious vision losses [19].

Figure 2.6: A Fundus image showing the retina detached from the eye posterior pole [15].

2.2 Treatment

The treatment for diabetic retinopathy in early stages, goes through the control of the blood sugar and the blood pressure by reducing the intake of fats, as any patient with diabetes should do. To prevent the onset of the disease, ocular exams should be performed regularly [20]. In more severe cases more invasive treatments are necessary. Some examples of them will be numbered and briefly explained below:

- Photocoagulation :

  It is a therapy that can be used to prevent the evolution of diabetic retinopathy, from non-proliferative to proliferative. It destroys the new vessels and seals the vessels that leak fluids and other substances. In macular edema, for example, the objective is to avoid the extravasation of more liquid, for which the vessels are sealed at the periphery of the macula [21] [20].

- Vitreoretinal surgery :

  The vitreoretinal surgery consists on removing the blood released in the vitreous hemorrhages and the vitreous humor itself. The vitreous humor is replaced by a gas or silicone oil. This surgery is applied in more advanced cases of proliferative diabetic retinopathy in which there are bleeds in the vitreous humor and retinal displacements. It is important to notice that vessels which cause retinal displacement are also removed [22] [20].

- Antiangiogenic Drugs :

  Drugs that inhibit the Vascular Endothelial Growth Factor (VEGF). Often used, preventing the creation of new vessels. Are mostly used to prevent the progression of proliferative diabetic retinopathy and usually are delivered through an intravitreal injection [23] [20]. Alongside with its neovascularization preventive capabilities, nefarious secondary effects like hypertension or impairment of wound healing can appear [23].

2.3 Diagnosis

Accessing the retina can be achieved through ophthalmoscopes, Optical Coherence Tomography (OCT) and fundus cameras. The impossibility to detect early-stages of DR [13] and the small field-of-view obtained with the opthalmoscope through a mydriatic-acquisition [24] alongside with the inability of the OCT to allow the direct observation of blood vessels, make fundus cameras the preferred method for DR screening [13]. More recently, the features of handheld fundus camera prototypes have increased significantly when compared with the traditional tabletop fundus cameras [25], proving as an helpful instrument in the diagnosis of many pathologies related with the retina and facilitating telemedicine applications [26, 27]. As the prototype designed during this thesis is a

fundus camera, the next subsection will explain those more specifically. The Figure 2.8 shows an example of a fundus photograph.

2.3.1 Fundus Camera

A fundus camera is a device based on indirect ophthalmoscopy principles and because of that, allow a considerable FOV without pupil dilation (Figures 2.7 and 2.8). Pupil dilation is usually achieved by the use of mydriatic agents which are usually uncomfortable for the patient [28].

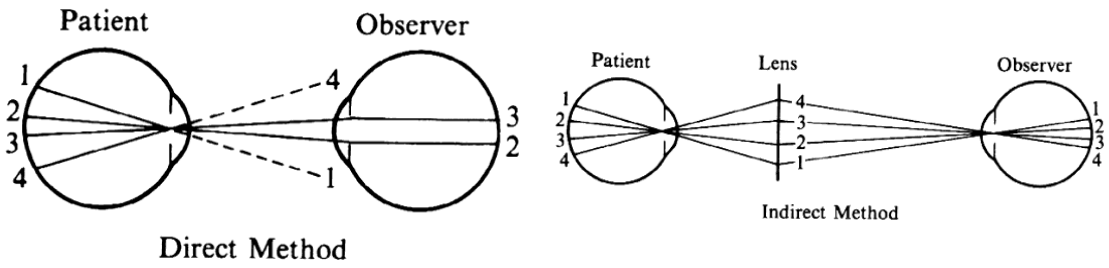

a Direct Ophthalmocscopy Method [29]. b Indirect Ophthalmocscopy Method [29].

Figure 2.7: Illustration of the comparison between direct and indirect opthalmoscopy methods. As can be seen by the usage of a condensing lens between the observer and the patient the Field of View can be increased[29].

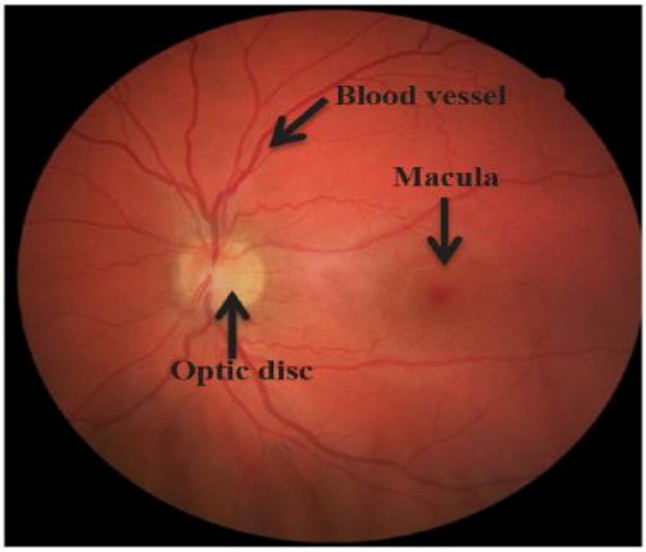

Figure 2.8: Eye Fundus image where Blood Vessels, Macula and the Optic Disk can be seen [30].

Over time, the usefulness of the fundus camera has also been tested in other medical

fields, with positive responses in Neurology (by relating retinal problems with strokes and cognitive problems) and in the assessment of cardiovascular risks, among others [31, 32].

A handheld portable fundus camera can also be a crucial tool in the development of telemedicine, which can be defined as the consultation between physicians or between physicians and patients by means of telecommunications [31]. The efficiency of this field is very dependent on the capacities and quality of the healthcare technological equipment. In this case, when the fundus examination can be performed by non-specialized individuals with a high success rate, the fundus camera becomes a valuable tool for the evolution of distance monitoring [31]. This monitoring, in addition to being extremely useful in hospitals, reducing waiting time, is fundamental in less developed areas or in patients with limited access to specialized care. As far as ophthalmology is concerned, telemedicine presents high success rates even when compared to the traditional on-site examination, being its main problem of implantation, the privacy protection and the confidentiality of the photographs obtained [31, 33].

2.4 Related Work

The improvement on the capabilities of handheld devices described in the subsection 2.3.1 led to a variety of different approaches. Some examples that reflect the recent scientific development are:

- Nonmydriatic Fundus Camera Based on the Raspberry Pi® Computer: Uses the Raspberry Pi® camera module coupled with a Condenser Lens to perform fundus imaging with a very low production cost [34].
- Eye-Selfie: By the usage of internal fixation points as targets, allows an acquisition of the fundus photograph, entirely self-performed by the patient [35].

As for ophthalmic devices available in the market, some prototypes are described next. The following reviews are based on information provided on the companies websites [36–38].

2.4.1 D-Eye Portable Retinal Imaging System

The D-EYE (Figure 2.9) is a smartphone coupled system which allows regular eye screenings, giving information about potential eye diseases and capturing images for future evaluation of each patient's medical condition. The features allowed are :

- Field of View up to 20º with pupil dilation;
- Field of View up to 6º without pupil dilation;
- Portable, requires no external power or light source;

- Ergonomic;
- Removes corneal reflexes;
- Store patient history in a file;
- Allows the review of pre and post-treatment images;
- Sharing of images;
- Compatible with all versions of the Iphone after the Iphone 5.

Figure 2.9: [Image of the D-EYE Ophthalmoscope coupled to an Iphone [36].

Although the D-EYE system is ergonomic and has great ease of use, it has a large gap, as previously mentioned, present in all ophthalmoscopes. An acceptable FOV is only obtainable through the use of mydriatic agents. In practical terms it allows the diagnosis of diabetic retinopathy only in advanced stages. There is the need of an external applicator to attach to the mobile phone at a cost of 99.00€. The cost of the device is 395.00€, thus having a total price of 494.00€.

2.4.2 Volk InView - Iphone Fundus Camera

The Volk iNview (Figure 2.10) is a fundus camera attached to a smartphone that allows the acquisition of retinal images. The free download application allows an automatic image capture during a query, choosing the most focused and defined images for fast acquisition. The application is secure in that it is encrypted with a password, ensuring, even in case of loss or theft of the Iphone, the confidentiality of the images.

Features:

- Free smartphone App;
- 1 Megapixel resolution with a static FOV of 50°;
- 80° dynamic imaging of the periphery of the retina;
- Both manual and automatic acquisition modes;
- Requires a 5mm pupil;
- Storing and uploading from the Iphone to the computer;
- Compatible with 5S/6/6S versions of the Iphone and with the Ipod Touch (Gen6);
- Compatible with all versions of the Iphone from the Iphone 5.

Figure 2.10: Image of the Volk Inview coupled to an Iphone [38].

Costing 1.495.00$, is the lowest costing solution, supplied by Volk. The low resolution and the need of pupil dilation are the main problems in this device.

2.4.3 Volk Pictor Plus

Pictor Plus (Figure 2.11) is a portable system that allows a non-mydriatic and high resolution acquisition in both bright and dark environments. These features enable the accomplishment of post-treatment follow-up and accurate diagnose. In addition to the retinal module, responsible for the image of the fundus, there are, an anterior module that allows the imaging of the eye anterior segment, a fluorescence angiography module that allows a highly defined visualization throughout the angiogram, an otoscopic module that allows examination of the auditory system and a dermatoscopic module.

- Portable (weights 0.45 kg);
- Image uploading to any Personal Computer or mobile device;
- 40° field-of-view in the Retinal module ;
- 9 Fixation Points for imaging of several retinal areas;
- Non-mydriatic;
- Possibility of red-free imaging;
- Both manual and automatic acquisition modes;
- Angiography module.

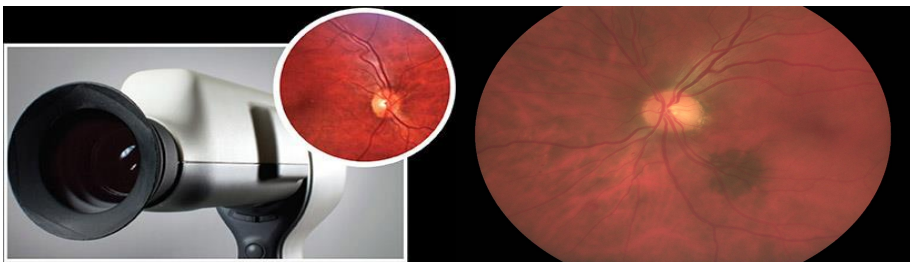

a Volk Pictor Plus fundus camera. b Fundus Image acquired with the Volk Pictor Plus.

Figure 2.11: Volk Pictor Plus [37].

At the date of the realization of this dissertation costed 9.995.00$. The Pictor Plus is a complete device that can be really helpful in several pathologies. The only main outcome ends up being the high price.

2.4.4 Fraunhofer EyeFundusScope

Before the beginning of this work, a prototype had already been developed by Fraunhofer. The system proposed differs from the previous approaches by using a smartphone for non-mydriatic retinal image acquisition. The use of a smartphone instead of custom electronic devices for image capture and processing allows a substantial decrease in costs while allowing for a very high image quality and resolution, thus guaranteeing the cost-effectiveness of the overall solution.

Although, the amount of dispersion and the existence of undesired reflections, caused by the absence of stops and by the prototype's inner surface not being completely absorbent, makes it harder to acquire well-focused images. The size and the impossibility of a continuous distance adjustment between components were other problems in this prototype.

Figure 2.12: Image of the previous prototype developed by Fraunhofer Portugal AICOS.

Due to the limitations presented by the prototype, a new compact optical system allowing a 40° FOV and considering a pupil of about 4mm (ensuring a non-mydriatic acquisition) will be designed as well as a smaller mechanical case for support of the new optical system, with a inner surface ensuring the absence of reflections.

Chapter 3

Introduction to Optical System Design

To design an optical system, a wide background knowledge, namely, in the field of Optics must be taken in account. In this chapter, several optical principles and tools, are explained and described. To understand the simulation software a small guide on the use of BEAM IV is presented as well as the simulation process tools with the description of the two ray tracing models needed for the evaluation of the capabilities of the optical system. As for the lenses, the types of lenses used during this work will be addressed along with a small description of existent optical aberrations caused by them.

3.1 Ray Tracing

Ray Tracing can be defined as a technique for image synthesis that consists in the systematic computation of the progression of rays of light through an optical system [39].

When the capacities of the computers weren't sufficient, the physicians plotted on paper the path taken by the rays, starting in a light source and then passing through the optical components. In the early 1970's, when the machines got fast enough, the optical modulation became available using computers and the appearance of a variety of software, made the ray tracing one of the very first numerical activities to be adapted to the computer [39]. One of the softwares is BEAM IV described in the following section.

Nowadays, Ray Tracing can be divided in forward ray tracing and backward ray tracing [40]. In the forward ray tracing, it is considered that the rays leave the light source and then are traced passing over the set of surfaces in the optical system. The backward consists in the inverse process. It considers that the ray start is in the goal surface and goes back to the light source. Both methods will be used along this work.

3.2 BEAM IV

BEAM IV is a table driven ray tracer software provided by Stellar Software. Being table driven means that the only inputs that need to be supplied to the system are text files containing tables.

This tables can be divided in different types, discriminated by the extension of the respective text file, being :

- Optics tables (.OPT).
- Ray Tables (.RAY).
- Medium Tables (.MED).

3.2.1 Optics tables

Describe the components (lens, mirrors...) of the optical system to be traced, presenting a set of optical characteristics for each component. These characteristics provide a realistic simulation of the components and make BEAM IV a reliable tool for the design of optical systems. The result of its usage can be seen in figure 3.1 as there is presented the table for simulation of an aspheric lens with a diameter of 30 mm and a goal surface at its focal length. The figure 3.1b shows the layout computation of the table. The following variables are the ones considered along the work progress in this thesis.

- **Type**:

  Specifies the type of each surface. Only the first letter is taken in account by the software. The different types allowed are lenses (represented by an l), mirrors (represented by an m), irises (represented by an i) or goals (final surface, represented by any initial letter, different than the previous ones). An Iris is a surface that don't change the ray direction only defines maximum and/or minimum radii of ray passage.

- **Index**:

  Refractive index of the medium approaching the surface. The default is 1.0.

- **X, Y, Z**:

  Lab coordinates for the center of each surface.

- **Diameter**:

  Diameter of the outer periphery of the surface.

- **T, P, R** :

  Lab coordinates for Tilt, Pitch and Roll angles in degrees.

- **Curv** :

  Curvature of the surface; Value = 1/radius of curvature.

- **Asph** :

  Asphericity is the departure from the spherical profile of a surface. Really helpful for the simulation of aspheric lenses, described in the section 3.4, and used throughout this dissertation.

3 surfaces Slah-Mounted Aspheric Lens 30mm.OPT

Index	Z	Diam	Type?	Curv	Asph
1.00	0.00	30.00	Lens	0.0495049	-1
S-LAH64	9.70	30.0	Lens		
	30.85561?	30	Goal	0	-0

a .OPT Table for the simulation of the lens.

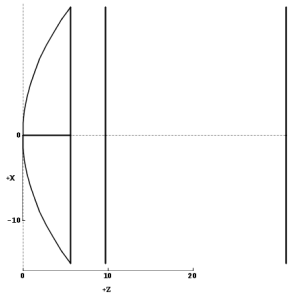

b Diagram of the Aspheric lens described using the Layout BEAM IV tool.

Figure 3.1: Computation of an S-LAH64 Aspheric Lens with 30 mm ϕ.

3.2.2 Ray tables

The input data supplied in these tables describes how the system is to be illuminated, by reporting the initial attributes of the light rays. Its importance is reflected in the amount of output data provided by them, informing not only the position and direction of the rays on the final surface, but also at any intermediate component. These features make Ray Tables the most relevant, in summarizing the results of any trace.

The implementation of the rays in the optical system leads to a much easier to interpret representation, as can be seen in Figure 3.2. The description of the used variables is presented next.

- **Input data**:

  The variables for the input data are the wavelength, specifying the wavelength for each ray, and the coordinates for ray start, having the pair (X0,U0) for the position and direction along the x-axis, (Y0, V0) for the y-axis and (Z0, W0) for the z-axis, respectively. The coordinates for the direction are the tangent of the angles rays make with the axis. For example, to compute a ray whose direction is of 20º with the x-axis, the U0 coordinate should be tan(20°) = 0.363.

  As input data it is also possible to define the goals with the variables Xg, Yg, Zg, Ug, Vg and Wg, representing the positions and directions that the user wants for each

ray. The goals are very important with some features like the Auto-Adjustment and the In-Out, described hereinafter.

- **Output data**:

  As mentioned before, the ray table can be set up to receive selected output data from any ray trace. To do this, appropriate output field labels need to be in the table header. The labels for the position at any surface are labeled with the axis and the number of the surface, for example, if one wants to know the position of the ray along the x-axis in the third surface, the label is X3. To have information in the final surface, the label is simply the label of the variable (X,Y,...) followed by the f letter (Uf for example, asks the software for the final direction of the ray relating to the x-axis). Other really important label is Notes, whose outputs describes the final destination of the ray. If the rays reach the final surface, the output is OK if they don't, the output informs on where and why the rays struggled (mis for missing surface, Dia for intercepting a surface beyond it's outer diameter...).

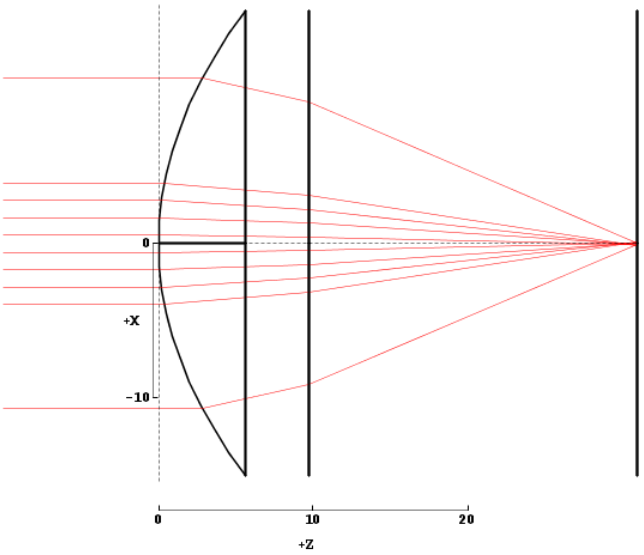

Figure 3.2: Diagram showing the simulation of the optical system described in Figure 3.1 with the addition of a .RAY Table.

3.2.3 Medium tables

Medium tables, despite not being essential to the optical design, can help a lot in turning it more realistic, by the allowance of polychromatic ray traces. These tables provide a collection of up to 999 glass records that hold the refraction data for several wavelengths from Near Ultraviolet to Near Infrared regions of the electromagnetic spectrum. It is possible to add new glasses as well as select ones from the default tables provided by

BEAM IV. The creation of new tables is possible and allows the selection of only the relevant glasses for each project.

3.2.4 Helpful BEAM IV Tools

Once the tables are defined, BEAM IV provides several tools in the RUN Menu that allow the understanding of the capabilities of the system modulated. The ones used during the realization of this thesis are the following.

- Layout:

  When selected, this tool simply shows the drawing of the system with the possibility of seeing different perspectives at different distances from the system (Zoom In and Out). It was the used tool to get the diagrams from figures 3.1 and 3.2.

- InOut:

  As the name suggests, this tool gathers the inputs from the tables and by the computation of the rays fills the output information on the ray tables (Notes,Xf,Uf...). When there are goals defined this feature also calculates the RMS, root mean square deviation, between the final coordinates and the goals.

- Plot 2D:

  This function provides a way to view relationships between any two ray trace variables. It is really important to show the arrival positions of the rays at the final surface of the optical system. In this project it was used with the Random tool so the uniformity of the illumination could be checked.

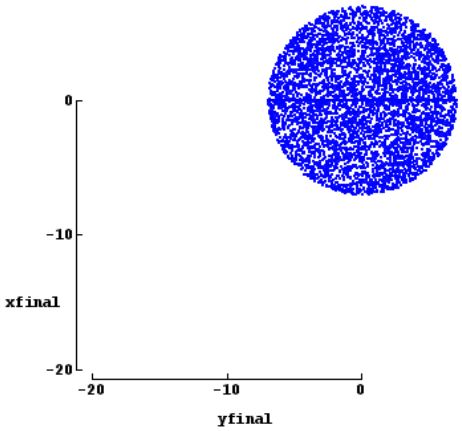

Figure 3.3: Example of the use of Plot 2D with the Random command.

- Histo 2D:

  The Histo 2D is a view of the relative frequency of any pair of ray variables. During this project was used in the same way that the Plot 2D, also coupled with the Random command.

- Random:

  The Random tool fulfills gaps between the rays defined in the Ray tables. Five probability distributions are available: the most common is the uniform distribution which gives equal probability for all ray start values within your start range. Cosine is centrally peaked, and Quartic Bell is bellshaped and more concentrated. Gaussians and Lorentzians offer specified concentration = half width of your span divided by the 50% probability width of the distribution. In this project only the uniform distribution will be used. An example of its use coupled with Plot 2D is shown in figure 3.3.

- AutoAdjust:

  Really helpful in the setup of some continuous parameters, like the Radius of Curvature or the positions of the surfaces and the rays. With this feature it's intended to diminish the value of the RMS. To autoadjust any variable only the tag letters must be changed. To change it independently from the rest of the system, the tag must be a question mark, to change a group of variables in the same way they need to be tagged with the same letter. Although it only works when the rays reach the final surface. If they don't, this command cannot be executed.

3.3 Optical Aberrations

To be in agreement with the optical capabilities needed there is the need of a system with minimized aberrations. To achieve it, first, some knowledge about optical aberrations and the different existent types is necessary. An optical aberration can be defined as the existence of different focal lengths for different rays of light when passing through the same lens [41]. Can be divided in the following groups :

- Chromatic Aberrations:

  Consist in the existence of different focal lengths for rays of light of different wavelengths. Are caused by the different refractive indexes any transparent material demonstrates for different wavelengths [42]. The medium table in Figure **??** demonstrates the refractive index variation.

- Symmetrical Monochromatic Aberrations:

  May also be called longitudinal spherical aberration. The symmetrical aberrations can simply be described as aberrations caused by rays of light with the same wavelength, passing through the periphery of the lens intercepting the optical axis closer

to the lens than the paraxial rays [41]. Usually, representative in lenses with a great diameter.

- Asymmetrical Monochromatic Aberrations:

  The Asymmetrical Monochromatic Aberrations are caused by rays with a direction that doesn't match the optical axis, which can also be called off-axis rays. One of the different kinds is named Coma due to the "cometlike" appearance of the image produced [41] and will be addressed later on this dissertation. The Figure 3.4 demonstrates the formation of Coma.

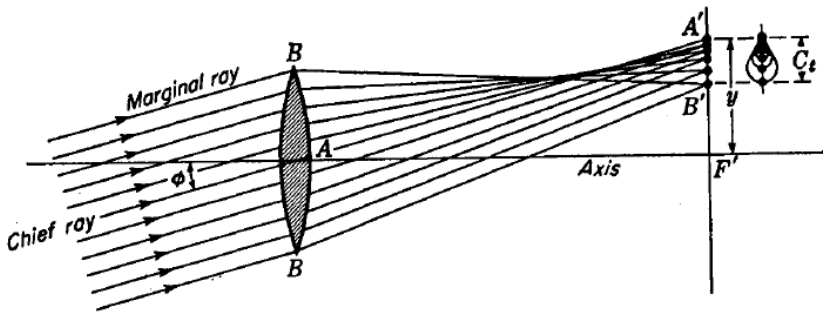

Figure 3.4: Coma explanation. The rays passing through the center of the lens are focused in a different region than those passing through the periphery (called marginal rays in the figure). The further from the center, the further from the chief ray focal point (A'), the rays will be focused [41].

As the desired system only comprises 3 lenses, the minimization of the aberrations will be attempted with the use of high quality components, with spherical aberration correction.

3.4 Types of Lenses

To reach the best optical system, several lenses were tested, namely :

- Plano-Convex (PCX) Lens:

  Lenses composed of one planar and one convex surface having a positive focal-length. Can be employed to converge collimated beams or collimate light from a point source.

- Bi-Convex Lens:

  Lenses composed of two convex surfaces. Can be used in many finite imaging models but as can be seen in Figure 3.5 lead to many spherical aberrations.

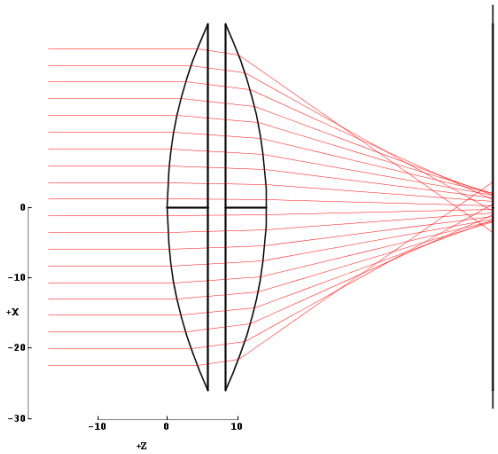

Figure 3.5: Bi-Convex lens showing too many aberrations.

- CNC-Polished Aspheric Lens:

  Lenses that provide a sharp image focus while minimizing image aberrations. Composed by one elliptical (non-spherical) surface characterized by an Aspheric coefficient, usually described with the letter k, related with the shape of the surface. These surfaces major contribute is in the minimization of monochromatic aberrations. Other of the advantages of these lenses when compared with others is that they are available in the market with largest diameters, providing a bigger numerical aperture.

- Achromatic Lens:

  Lenses whose main goal is to prevent the occurrence of chromatic aberrations when used in the visible part of the electromagnetic spectrum, allowing really small focal length shifts for radiation at different wavelengths, as can be seen in Figure 3.6. The system doesn't present many chromatic aberrations so these lens were excluded from the final optical system. Other reason for excluding them, is related with the fact that the achromatic lens available in the market don't have the sufficient capabilities (Diameter and Dioptric power) to allow the imaging of 40º of retinal area.

- Best-Form Lens:

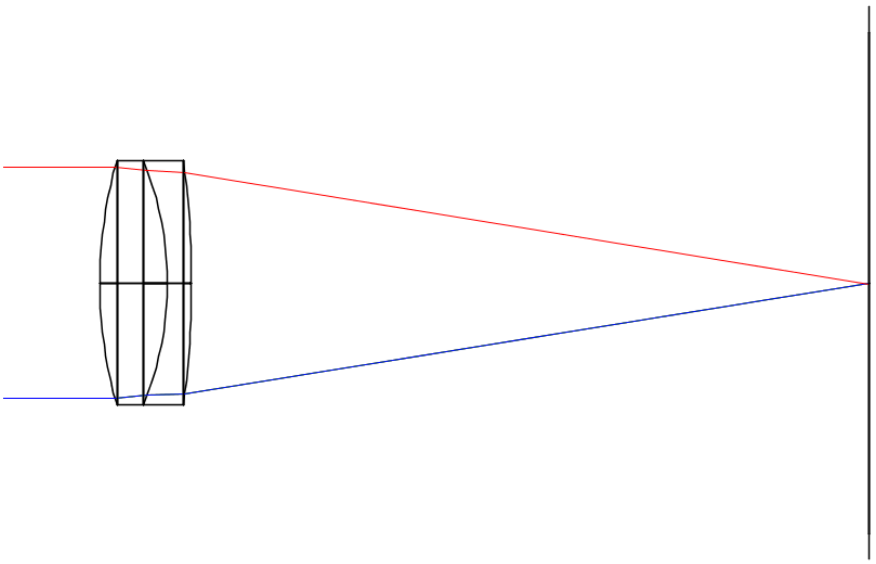

Figure 3.6: Achromatic lens performance, showing similar focal length for different wavelengths.

Lenses characterized by 2 spherical surfaces but with a combination of curvatures that minimizes the spherical aberrations.

3.5 Ray tracing models

3.5.1 4-Extremes Model

This model assumes that the light source emits from a single point with a certain aperture previously declared by the manufacturer. The value usually comes declared as presented in Figure 3.7 and the angles for which the relative luminous intensity is bellow half the maximum intensity can be neglected.

So, for example, for the LED with the graph in Figure 3.7 the four extremes model describes four rays beginning at the exact same position, having the angle of 30º as the maximum deviation from the normal. To implement the rays, it is needed to calculate the tangent of 30°, which is equal to 0.577.

Considering this value, the table for the emission rays of this LED is the one displayed on Figure 3.8. As can be seen in the table the initial position is the same for every ray, and the only difference is in the direction. The directions are the positive and negative x-axis and the directions of the positive and negative y-axis. In this design, the z-axis is parallel to the optical path.

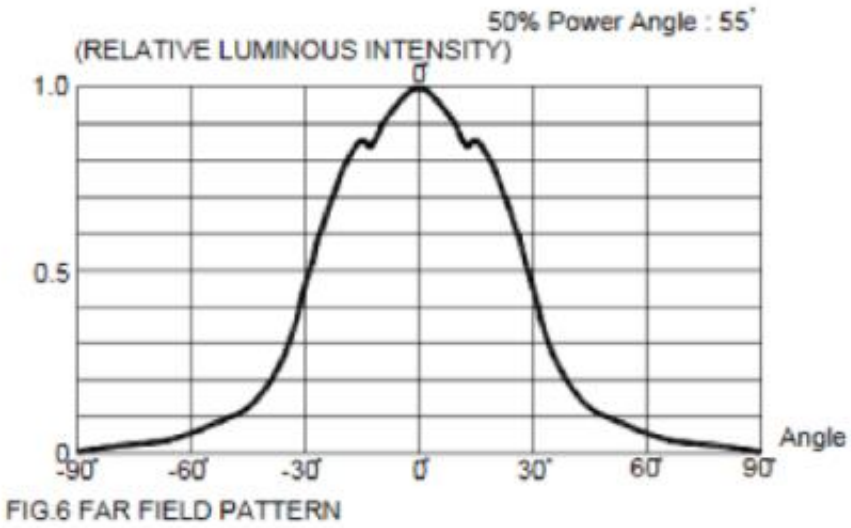

Figure 3.7: Graph of the luminous intensity of the LED relative to the angle with the normal.

8 rays PCXrodado.RAY

X0	W0	V0	U0	notes
0	+1	0	0.577	
0	+1	0	-0.577	
0	+1	0.577		
0	+1	-0.577		

Figure 3.8: Ray table with rays for the 4-extremes model.

3.5.2 Parallel Rays Model

This model assumes that when two rays focused at some finite point reach a lens, they are collimated and leave the lens with the same direction and parallel with each other. In Figure 3.9 an application, relevant for the work presented in the next chapters, of this model is demonstrated, showing rays focused at two different points in the retina, leaving the pupil parallel. The initial direction is the widest allowing the passage through the pupil. The module of Uf for both rays is 0.00007 which indicates that they are almost perfectly parallel, validating the approximation.

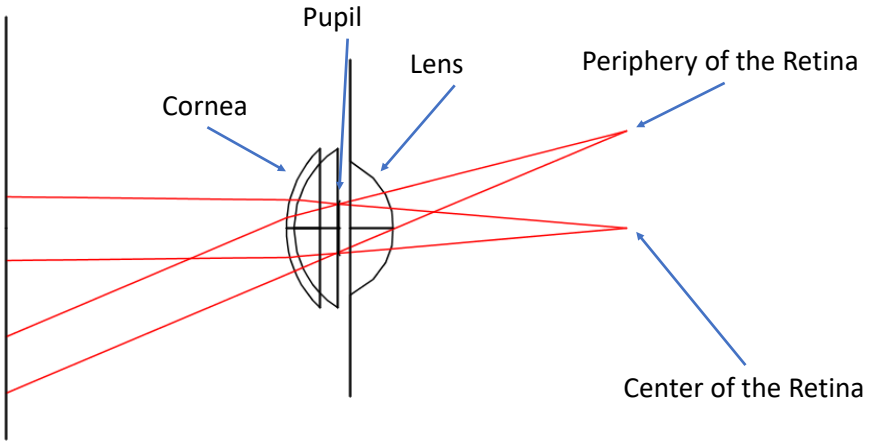

Figure 3.9: Illustration of the parallel rays model. In this figure rays are focused on the retina, leaving the pupil collimated and parallel.

3.6 Objective Lens Condition

As in most fundus cameras, for retinal illumination, there is a lens above the light source to collimate the rays and another lens to focus the rays. This lens that focus the rays before reaching the eye is called objective lens.

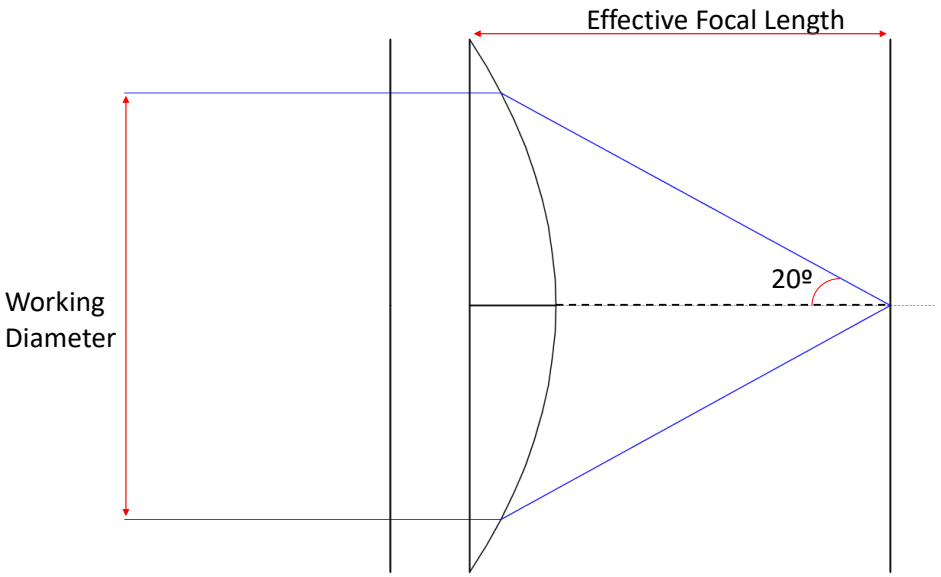

Figure 3.10: Diagram proving that for a 20°half-angle the relationship $\frac{WD}{2f}$ should be equal or superior to sin(20).

To obtain a field-of-view of 40° there is a constraint that the relationship $\frac{WD}{2f}$ should be superior to $sin(20°)$ (see Figure 3.10), where WD stands for Working Diameter and f means the effective focal length of the lens. As can be seen in the diagram in the fig. 3.10 one can be easily mislead to use the tangent, but the usage of the sine is justified by the fact that the lens principal planes must be regarded as curved surfaces when the rays reach beyond the paraxial region, as it is declared by the Abbe sine condition [43].

3.7 Fundus Camera Components

In this work, to diminish the production costs, only the fundamental components of a fundus camera were used. A field-of-view of at least 40° is desired, since this is generally considered an adequate tradeoff between sufficient retinal area imaged and enough resolution for analysis of finer retinal features, thus allowing clinical meaningful conclusions about eventual abnormalities.

A simple fundus camera setup is described in Figure 3.11, showing the fundamental components. The usage of a beamsplitter is needed in order to keep the coaxiality between the illumination and imaging optical paths. This means that the optical path for simulation, must be separated in two different paths. The illumination path, describing how the rays go from the light source (LED) to the retina and the imaging path, describing how the rays go from the retina to the sensor, in this case, the smartphone camera. The condenser lens is important in the collimation of the rays coming from the light source before reaching the objective lens. The objective lens is crucial for the entrance of the rays for the eye as its location and dioptric power is what defines where the pupil of the eye should be located (focal point) as the ocular lens is necessary for the focusing of the rays coming from the retina, in the smartphone camera.

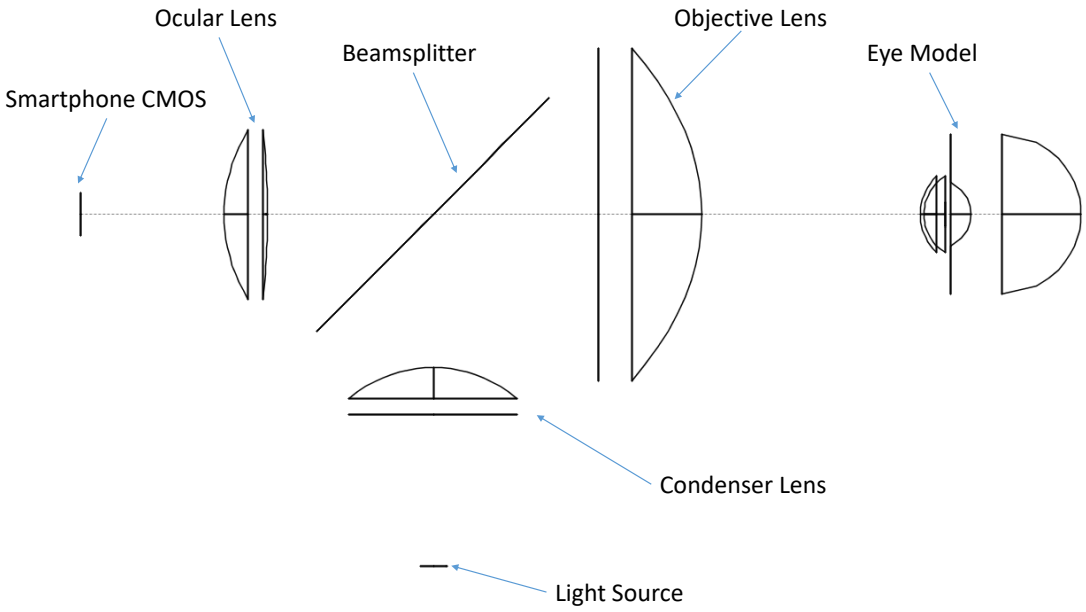

Figure 3.11: Illustration of the fundamental components in a fundus camera prototype.

Chapter 4

Optical System Design

In the present work, it is proposed a simple Fundus Camera optical system, using only 3 lenses, allowing a 40º field-of-view with minimized aberrations and no need of pupil dilation. In this chapter the simulation performed using BEAM IV will be described. The simulated systems will be, a model of the eye to accurately check systematic optical capabilities, the optical path taken by the rays, internal fixation points for different pupil alignments as well as adjustments needed for eyes with refractive errors.

Usually, to design a Fundus Camera the usage of a beamsplitter is needed in order to keep the coaxiality between the illumination and imaging optical paths. This means that the optical path for simulation, must be separated in two different paths. The illumination path, describing how the rays go from the light source (LED) to the retina and the imaging path, describing how the rays go from the retina to the Sensor, in this case, the smartphone camera.

4.1 Previous Optical System

Before the beginning of this thesis, there already was a fundus camera prototype. The optical system for this prototype is presented in Figure 4.1 and was composed by :

- A Visible LED:

  As a light source, a Visible LED emitting white light with 60º viewing angle was used, giving rise to a lot of dispersion.

- Volk 22D Pan retinal Lens (Aspheric Lens with 52mm Diameter) :

  The Volk 22D Pan retinal is a Bi-Convex aspheric lens, theoretically good for fundus imaging since it allows a wide Field-of-View 56º/73º at a working distance of 40 mm.

- Non polarizing Beamsplitter 50R/50T (35x35mm):

  The Beamsplitter has the purpose of separating one incident light ray in two separate beams. Being 50R/50T means that it splits the original ray of light into two different ones with half of the intensity of the original one. In BEAM IV, the reflective and transmissive strands must be simulated separately. For the reflective, the beamsplitter is considered a mirror and for the transmissive it is omitted.

- Edmund Optics Plano-Convex Lens 20 D (30 mm diameter)

  The Plano-Convex Lens is used as a Condenser Lens with a purpose of collimating the divergent beams coming from the light source.

- B + W 40.5mm +4 Close Up Glass Filter - NL4

  A Close-Up lens is a magnifying lens which allows a larger image scale.

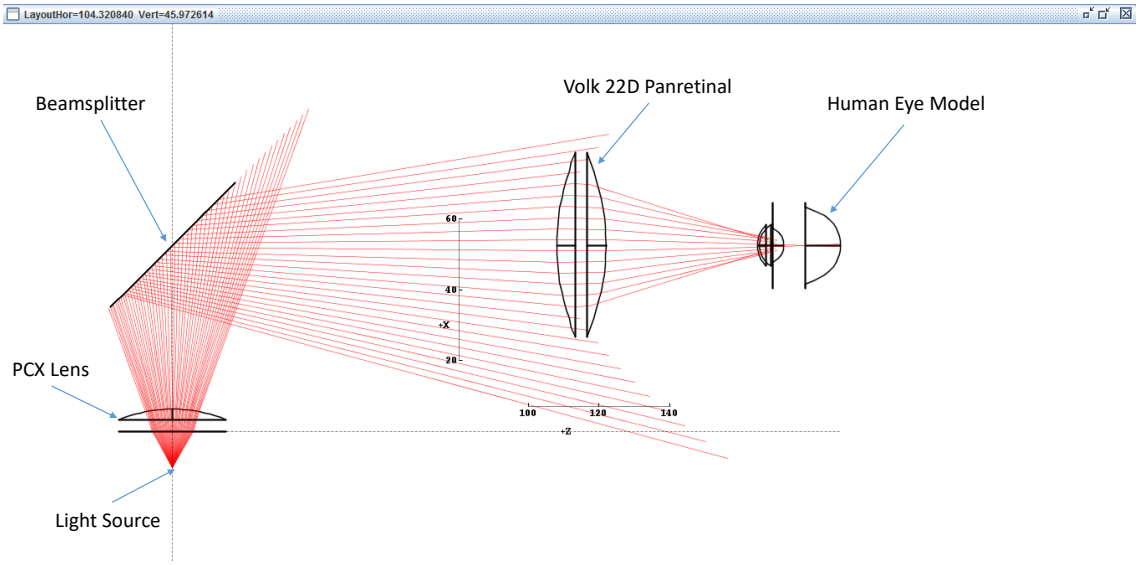

Figure 4.1: Original optical system.

Some manufacturers of the lenses used in this system, didn't provide information on some of the lenses characteristics as the Radius of Curvature and Asphericty coefficients, considering them confidential, so the diagram of Figure 4.1 is only an approximation and is not fully optimized. Features like the FOV and the resolution weren't measurable, although a lot of dispersion is noticeable in the representation. The dispersion wasn't completely corrected by the fact that the inner surface of the prototype wasn't able to absorb all the light. This problem can be solved by the usage of aperture stops, which are structures that only allow the passage of rays over a defined diameter. As can be seen by the comparison of Figures 4.1 and 4.2, the utilization of a stop improves the optical quality of the system by reducing dispersion.

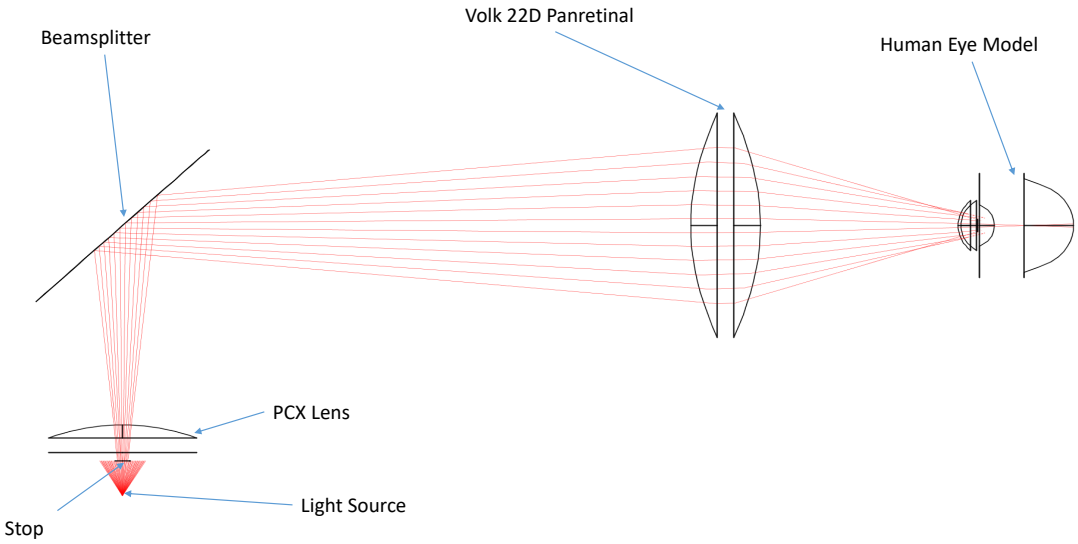

Figure 4.2: Demonstration on how the utilization of stops can prevent dispersion, in the previously developed optical system.

4.2 Human Eye Model

To guarantee a satisfactory field-of-view, an accurate model of the eye is needed. The eye has two refractive lenses, the cornea and the crystalline lens. Based on the literature [44] and following a similar approach to [45], a model of the eye was created in BEAM IV considering the radius of curvature, diameter and asphericity coefficients of all the structures relevant for ray tracing. The pupil has been designed with a 4 mm diameter to simulate a non-mydriatic acquisition and is coincident with the lens anterior surface. The chromatic aberrations from the eye were neglected as the change in diopters at different wavelengths were not considered significant in the scope of this work [44].

The defined structures of the eye, as represented in Figure 4.3, are:

- Corneal Anterior surface:

  Diameter = 11.50 mm
  Radius of Curvature = 7.75 mm
  Asphericity coefficient = -0.2

- Corneal Posterior surface:

  Diameter = 11.50 mm
  Radius of Curvature = 6.8 mm
  Asphericity coefficient = 0

- Pupil/ Lens Anterior surface:

Diameter = 4 mm
Radius of Curvature = 10 mm
Asphericity coefficient = -0.94

- Lens Posterior Surface:

  Diameter = 9 mm
  Radius of Curvature = -6 mm
  Asphericity coefficient = 0.96

- Retina:

  Diameter = 24 mm
  Radius of Curvature = 12 mm
  Asphericity coefficient = 0

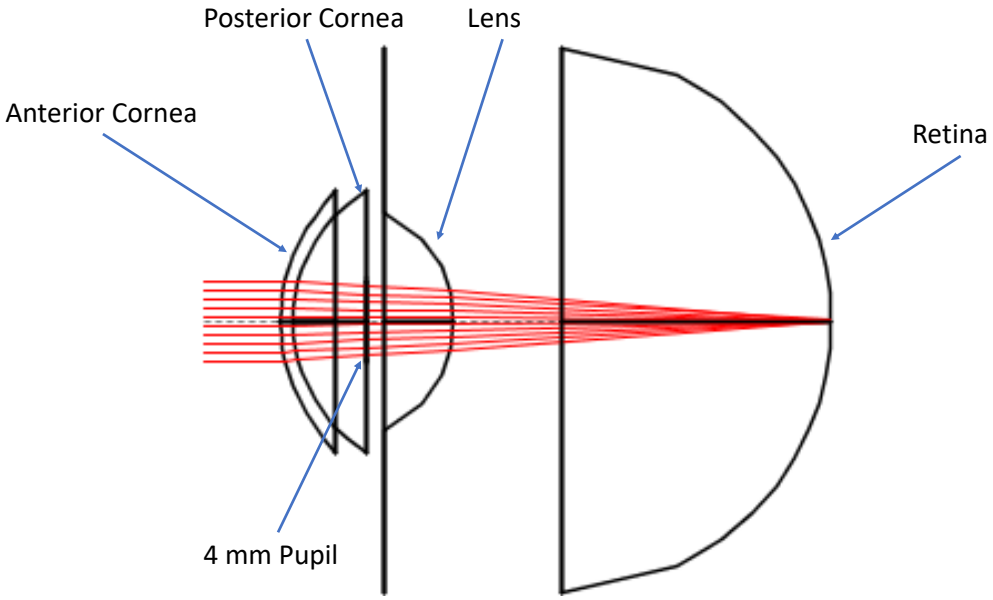

Figure 4.3: Eye Model designed using BEAM IV. Rays at infinity being focused on the retina.

4.3 Illumination Path

For the illumination path the main goal is a 40° field-of-view with a uniform illumination of the retina. The image is obtained using a white visible LED but, to allow a non-mydriatic acquisition, a Near Infra-Red (NIR) LED is used, helping the examiner to perform alignment of the device with the eye and to find the area of the retina to be imaged. As the NIR LED is simply used for guidance, only the Visible LED imaging and illumination capabilities were evaluated.

As in several handheld fundus camera designs [25, 46], there is a lens above the light source to collimate the rays and another lens to focus the rays. This lens that focus the rays before reaching the eye is called objective lens and it is where the simulations described in this dissertation began. The type of objective lens chosen should minimize spherical aberrations. This condition, coupled with the required numerical aperture (section 3.6), makes Aspheric lenses the only suitable option for the focusing of the rays when reaching the retina. After searching for a lens that fits these requirements the option ended up being a Thorlabs Aspheric Lens with 50.00 mm diameter, 40.00 mm focal length and SLAH-64 glass type, placed 25 mm ahead to the right of the center of the beamsplitter. For the collimation of the rays coming from the light source, the used Condenser lens was an Edmund Optics Plano-Convex Lens with 25.4 mm diameter, 38.1 mm focal length and N-BK7 glass type, placed 47 mm below the center of the beamsplitter.

To check the distance between the objective lens and the human eye, the plane where the rays were in focus was calculated. This plane is called the focal plane and is where the circle of confusion is minimum. In a theoretically aberration free-system, this is where the pupil should be placed to ensure that a great part of the rays reach the retina and are not reflected by the white surface of the cornea. These tests were performed for a blue light with 486 nm wavelength and are represented in Figure 4.4.

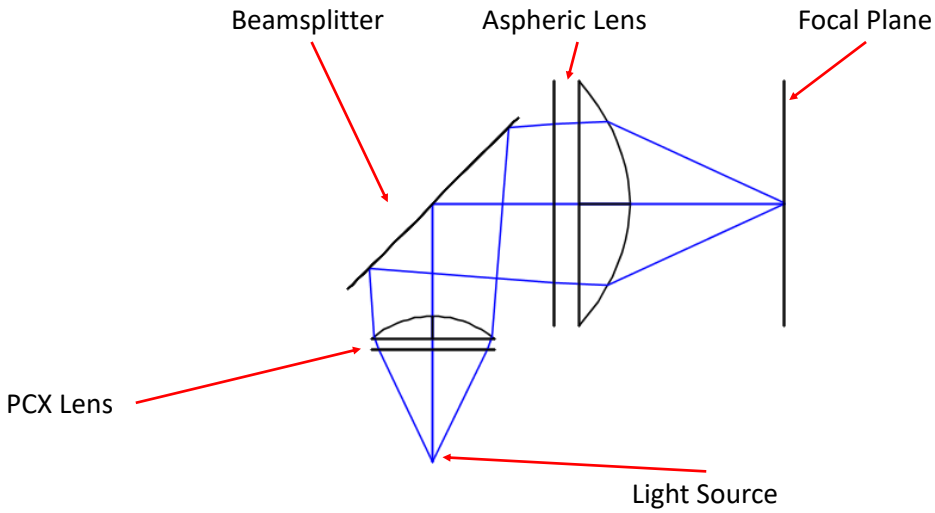

Figure 4.4: Diagram showing the focal plane where the circle of confusion is minimum for the system designed.

The measured distance from the curved surface of the objective lens to the focal plane was 31.5 mm.

The results of this setup can be observed in the fig 4.5 that shows an half-angle on the retina of 21° but lack in the uniformity of the illumination profile. This is explained by the intermediate rays reaching the optical axis further than the extreme rays, due to

spherical aberrations, resulting in a 40% transmittance. The existence of these aberrations is very usual in lenses with a great diameter as the one used as an objective.

A description on how the FOV was calculated is done on the annex II. The procedure for the calculation of the FOV will be the same throughout this dissertation.

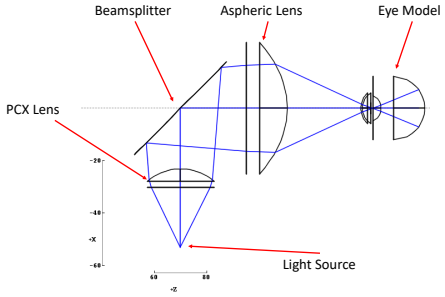

a Representation of the Illumination path.

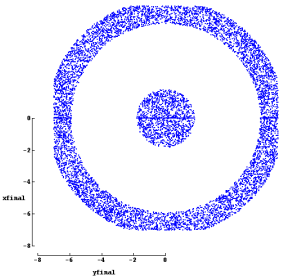

b Retinal illumination profile showing that the intermediary rays don't reach the retina, preventing a proper illumination.

Figure 4.5: Illumination path with eye at 31.5 mm from the objective.

Using the AutoAdjust tool it was possible to see that the pupil, to accomplish a uniform illumination of the retina, should be placed at 36.6 mm from the objective, this means the eye must be moved away 5 mm from the objective. Using this different configuration, 90% of the emitted rays reach the retina and the illumination profile is uniform, as can be observed in Figure 4.6. The half-angle on the retina calculated was 20.66° leading to a total field-of-view of 41.32°.

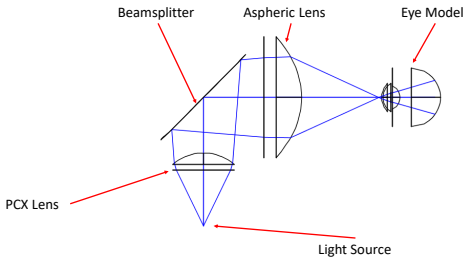

a Representation of the Illumination path.

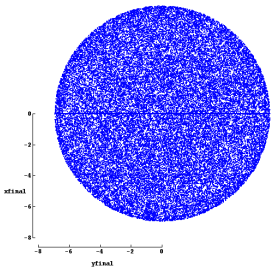

b Retinal illumination profile showing illumination uniformity.

Figure 4.6: Illumination path with eye at 36.6 mm from the objective.

In the previous diagrams, the simulated light source emits on a single wavelength (486 nm). As the white light emitted by the LED has a continuous emission spectrum, measurements at the other end of the visible spectrum are needed. It was concluded that for red light (656 nm) the system is also optimal with 92% of the rays reaching the retina with an half-angle of 20.57°, leading to a total field-of-view of 41.14 °. This slight difference occurs because the increment in the wavelength changes the refractive indexes

of the lenses, causing the rays to intercept the optical path in a little different position, than they do with a blue light. As the white light consists in the addition of several different wavelengths, a 92 percent efficiency at one end (red) and 90 percent at the other (blue) makes this system considerably reliable.

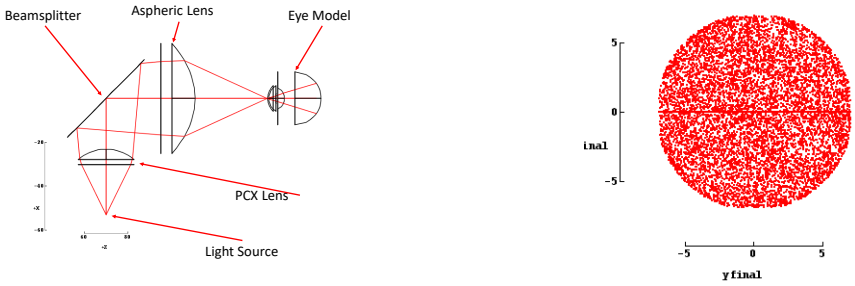

a Representation of the Illumination path

b Retinal illumination profile showing uniformity

Figure 4.7: Illumination path with eye at 36.6 mm from the objective with the LED emitting at 656.27 nm (Red Light)

4.4 Imaging Path

For the imaging path the key features desired are the almost complete fulfillment of the smartphone camera sensor and the minimization of aberrations. These characteristics can be verified using the parallel ray model. In order to perform a forward ray tracing analysis of the imaging path, two pairs of parallel rays were considered, one pair parallel with the optical axis and the other with 20° inclination. The distance between the rays, on each pair, was equal to the size of the pupil, 4 mm. The imaging path is presented in Figure 4.8.

The system was optimized for a LG Nexus 5X camera whose relevant specifications are:

- Horizontal angle of view : 68.2°
- Vertical angle of view : 53.1°
- Sensor size : 1/2.3"(6.17 x 4.55 mm)

The final optical system must guarantee that the vertical angle of view is mostly filled with the retinal image, in order to allow the highest possible retinal resolution, essential for the clinical analysis of fine features. The first solution tested was with the Aspheric Lens, described in section 4.3, as an objective lens and with a plano-convex lens with 40.0 mm of focal length and 25.4 mm diameter serving as an Ocular. The maximum diameter for the Plano-Convex lens to fit the scope of a compact system was defined to be of 25.4 mm.

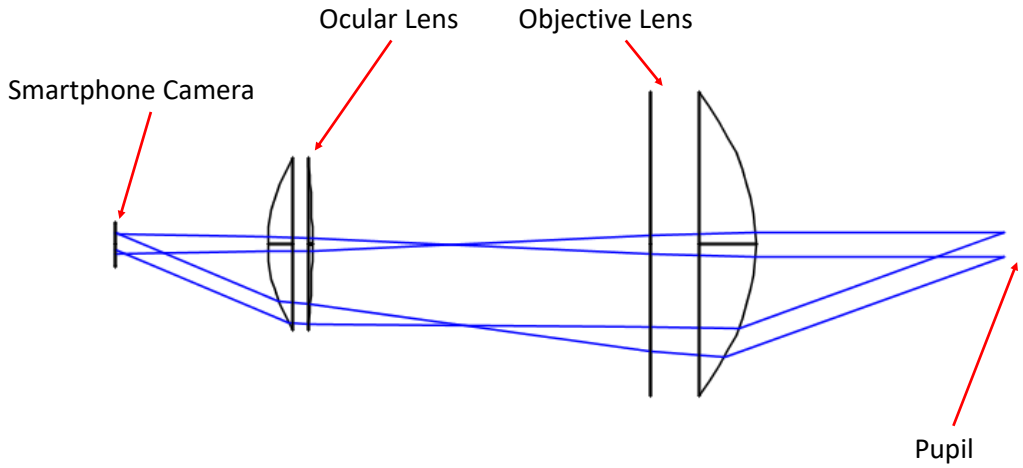

Figure 4.8: Diagram showing the Imaging path with the classification of each lens having in account the position.

The system achieved, represented in Figure 4.9 had very different inclinations on the CCD, one having 25.6º and the other having 23.2º.

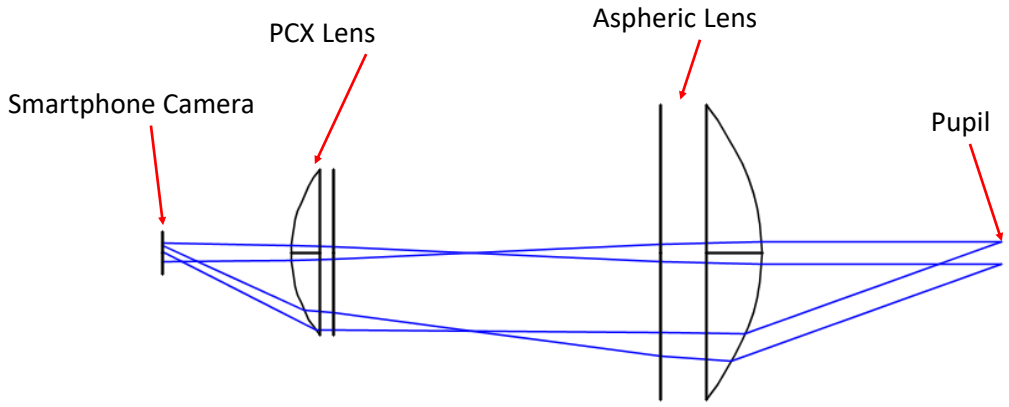

Figure 4.9: Imaging path with an Aspheric Lens and a PCX Lens simulation with the parallel rays model.

These aberrations are even more visible when backward ray tracing, describing the path rays take from the camera to the retina, is used. To simulate this path, a 4-extreme model was used but with different characteristics. The four rays in this case have all the

same direction, four at the extreme solution with 25.6º inclination and four at the center, parallel to the optical path. The rays start position is equally distant from the origin at the positive and negative directions of the x and y-axis. In a non-aberrative system both extreme and center rays should focus at a similar distance from the Ocular but as can be verified in Figure 4.10, that doesn't happen. This difference is problematic when the rays reach the retina, not providing a satisfactory image of the human eye.

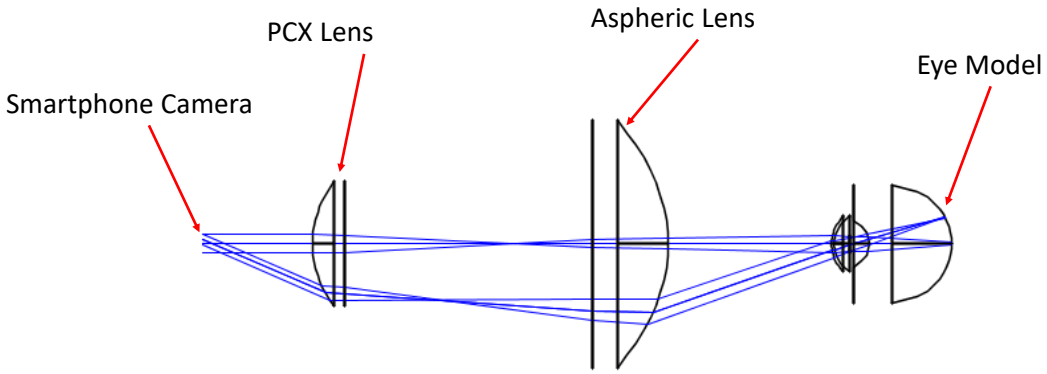

Figure 4.10: Simulation to check if a ray going from the smartphone CMOS parallel is focused on the retina. A PCX and an aspheric lens are used in the imaging path.

To correct the aberrations, as the Objective Lens already fulfilled the requirements for the illumination path, the Ocular Lens was changed. A Best-Form Lens with 40.0 mm focal length, 25.0 diopters and 25.4 diameter was tested. The aberrations were almost eliminated and the rays reached the smartphone camera parallel to each other, with an inclination of approximately 22 °, leading to an angular field-of-view of 44°. The diagram can be seen in Figure 4.11. The angle in this configuration is inferior to the achieved with the PCX lens as an ocular, but still wide enough to avoid a significant crop.

In this setup the distance between the smartphone CMOS sensor and the Best-Form Lens is 22 mm. The distance between the surface of the Best-Form Lens with less curvature and the planar surface of the Aspheric Lens is 50 mm and between the Aspheric lens and the eye is 33 mm. In Figure 4.12, using backward ray tracing, it is visible that the results were improved, comparing with the previous solution. The focusing of the image is a little after the retina for the center rays, as for the extreme rays is a little before.

This leads to a difference in the resolution at different retinal areas. With the adjustment of the distance between the eye and the Objective the optical quality in a specific area of the retina can be improved. The periphery resolution is improved by approximating the eye as the central resolution is improved by moving it away. As can be seen in

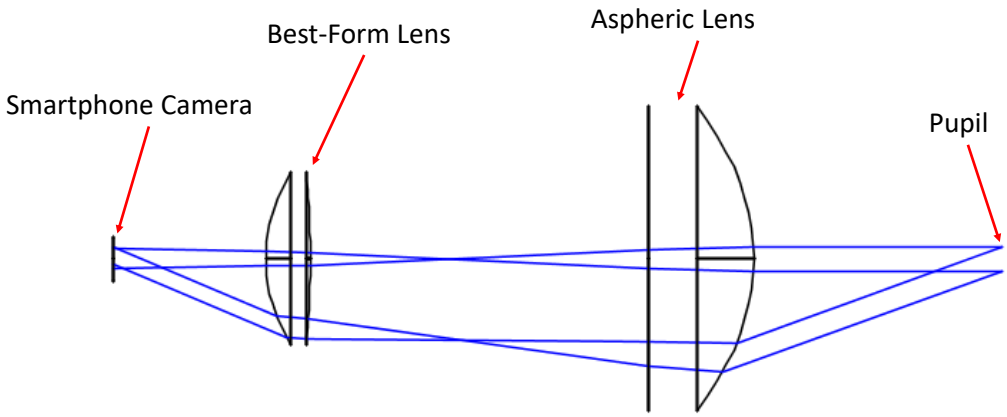

Figure 4.11: Imaging path with a Best-Form Lens as the Ocular Lens and an Aspheric Lens as the Objective, using the parallel rays model, showing better capabilities than with the PCX Lens.

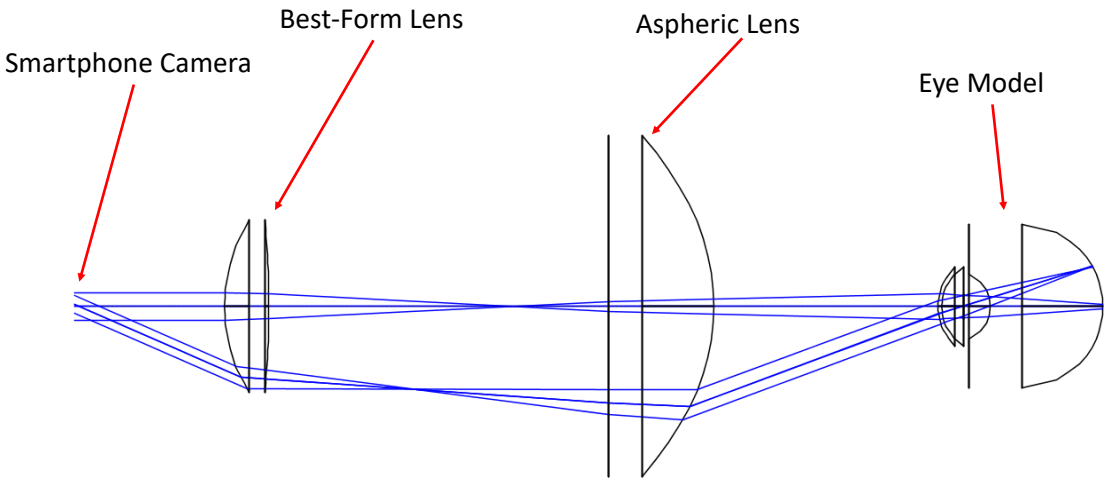

Figure 4.12: Diagram showing the simulation used to check if a par of rays leaving the smartphone CMOS parallel is focused on the retina. A best-form and an aspheric lens are used in the imaging path.

Figure 4.13 by moving the eye 4 mm away from the objective the focus in the center can be improved as for the extreme rays the best solution is accomplished by approximating the eye 1 mm to the objective, described in Figure 4.14. At the extreme rays an aberration type called coma (described in the section 3.3) is visible. These aberrations occur when the image is off-axis and result in a asymmetric image.

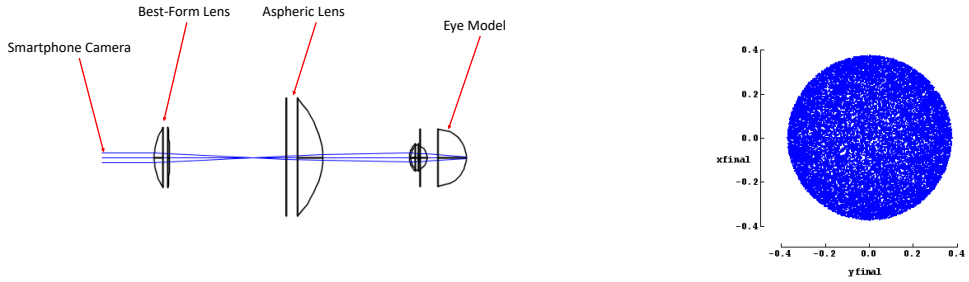

a Imaging path best solution for central rays.

b The minimum circle of confusion is obtained by moving the eye 4mm away from the center.

Figure 4.13: Imaging path demonstration for central rays. The eye is moved away from the system 4mm. The rays leave the Smartphone CMOS parallel and are focused on the retina. The figure on the left shows the minimum circle of confusion (≈ 0.3 mm) when reaching the retina.

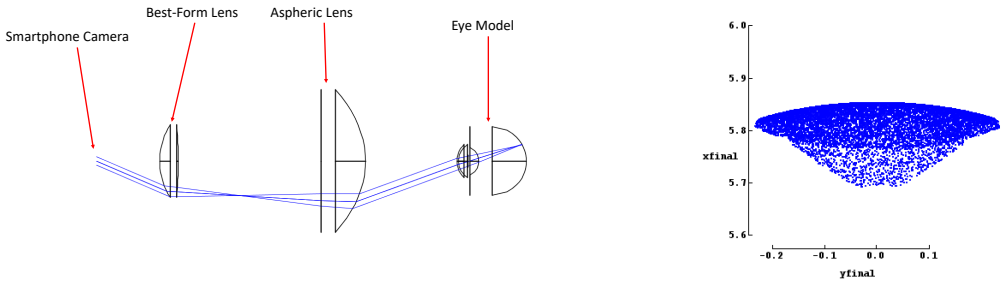

a Imaging path best solution for periphery rays.

b Periphery rays retinal profile

Figure 4.14: Imaging path best solution for periphery rays. The eye is 1 mm approximated to the system. In the periphery rays retinal profile is visible the existence of coma.

4.5 Imaging Path for Eyes with Refractive Errors

Eyes with refractive errors present different optical characteristics and so, the position of at least one of the lenses in the optical system must be adjustable to compensate this. As the smartphone camera is able to change its focus target distance, the refractive errors were modulated in the range of -5D to +5D. Since one of the possible cause of refractive errors is the size of the eyeball [47], for the modulation of Myopia the retina was moved 3 mm away from the refractive center of the eye. Concerning the modulation of Hyperopia the eyeball was shortened 3 mm. Considering that the eye refractive power is approximately 60 D [44], by the use of the equation I.2 for changes of -5D and +5D, the focal length will change +1.18 and -1.7 mm, respectively. The value chosen was 3 mm to give margin for slightly bigger refractive errors. In Figure 4.15, the system configuration for an eye without any refractive error is shown. In Figures 4.16 and 4.17 are presented diagrams showing the adjustments done to compensate these refractive errors. For the Myopic eye the error is corrected by moving the Objective Lens 5 mm away from the eye. Concerning the Hyperopic eye, the Objective lens is approximated 5 mm to the eye.

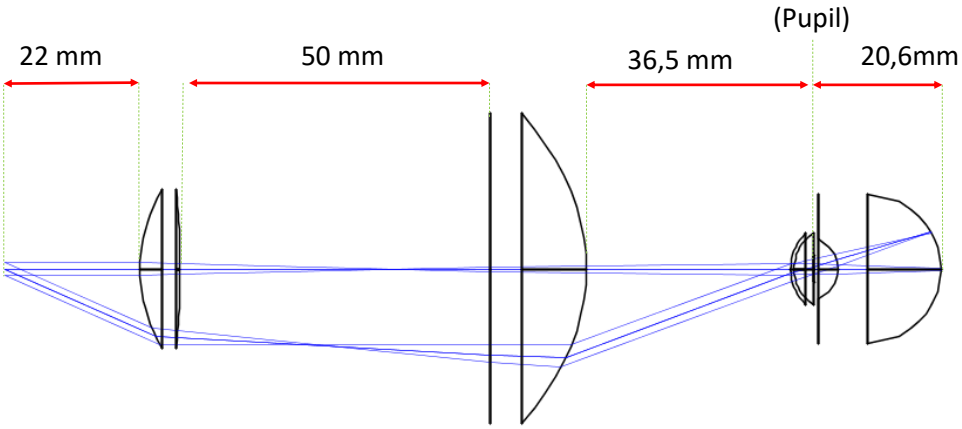

Figure 4.15: Diagram showing the distance between the components in the imaging path for an eye without refractive errors (Normal Eye)

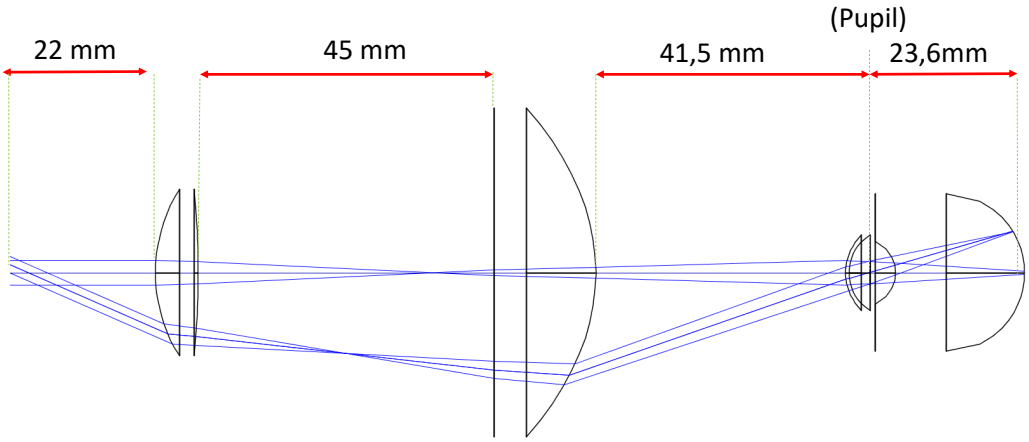

Figure 4.16: Diagram showing the distance between the components in the imaging path for an eye with shorter focal distance (Myopic Eye).

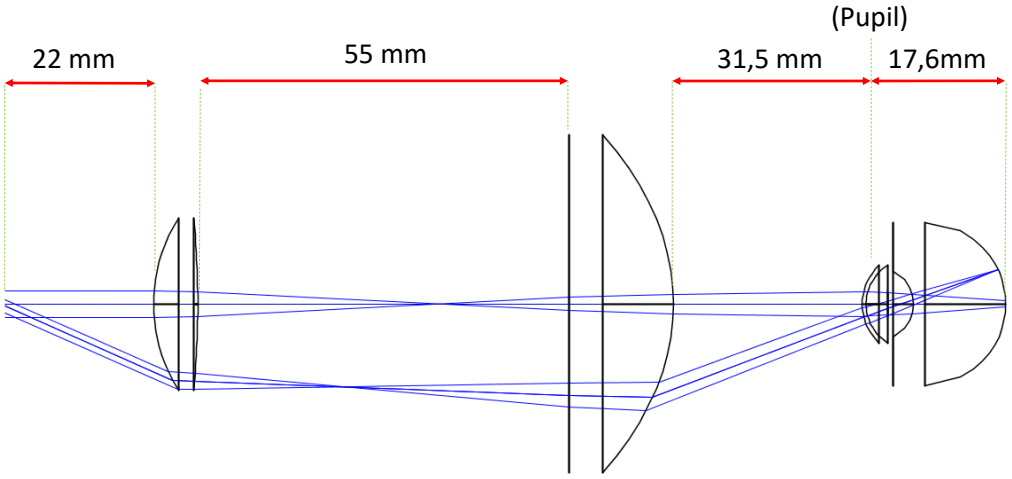

Figure 4.17: Diagram showing the distance between the components in the imaging path for an eye with longer focal distance (Hyperopic Eye)

4.6 Complete Optical System

With the illumination path and imaging path developed the complete optical system presented in Figure 4.18 has the following components [1] :

- Light Source (Visible or Near Infra-red LED).
- N-BK7 Plano-Convex Lens, 38.1 mm Focal Length, 25.4 mm ϕ, VIS-NIR Coated, 44,00€, Edmund Optics.
- S-LAH64 CNC-Polished Aspheric Lens, 40.0 mm Focal Length,50 mm ϕ, 392,00€, ThorLabs.
- Beamsplitter 50R/50T 50x50 mm, ($\approx$ 50,00 €).
- N-BK7 Best-Form Lens, 40 mm Focal Length, 25.4 mm ϕ, 39,00€, Thorlabs.

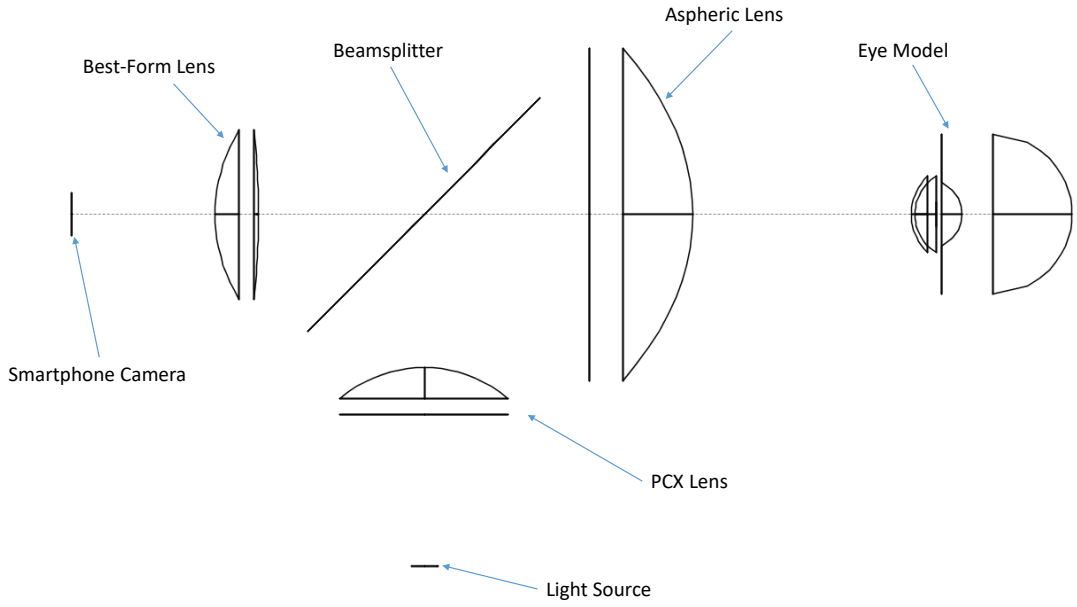

Figure 4.18: Complete optical system.

The utilization of aperture stops is dependent on the LEDs beam angle. The aperture can be used to stop the rays emitted by the LED at a wider angle than the necessary for a field-of-view of 40°, preventing reflections and the imaging of undesired areas.

The main features of the developed system are:

- About 40° field-of-view.
- Non-Mydriatic Acquisition, for a 4 mm pupil size.

[1] The prices date from June of 2017

- No significant aberrations (Spherical and Chromatic).
- Uniform Illumination of the Retina.
- Simple and affordable lens system.

4.7 Internal Fixation Points

A fixation point can be described as a visual target, very useful in many eye exams. By preventing major eye movements [48], allow the examiner to search for the best position, concerning the area of the retina that wants to be imaged. With this purpose, the fixation points are used with many ophthalmic devices. As external fixation points make the system less compact and with an external part that most of the times is more fragile (Figure 4.19), the fixation points designed for this project should be inside the mechanical case to allow an easy transportation with less risk to be broken. Other issue with the external fixation points is that they are useless for patients with only one functioning eye.

Figure 4.19: Demonstration of an external fixation point in a table-top Canon CR-2 PLUS AF Digital Non-Mydriatic Retinal Camera [49].

Besides the prevention of eye movements in the course of the exam, fixation points can be used to achieve a very interesting capability for a fundus camera that is the allowance of several pupil alignments. With the existence of several pupil alignments, several areas of the retina can be imaged.

A LEDs matrix is a helpful tool to ensure the existence of distinct fixation points, providing several targets. By turning on one LED of the matrix at a time and asking the patient to keep looking at the LED, the pupil is deviated and the light rays entering the

eye will allow the imaging of retinal areas deviated from the center. This characteristic coupled with the capacity on the smartphone application to stitch overlapping images can increase a lot the achievable Field of View. In Figure 4.20 is presented the stitching accomplished through the smartphone application developed by Fraunhofer.

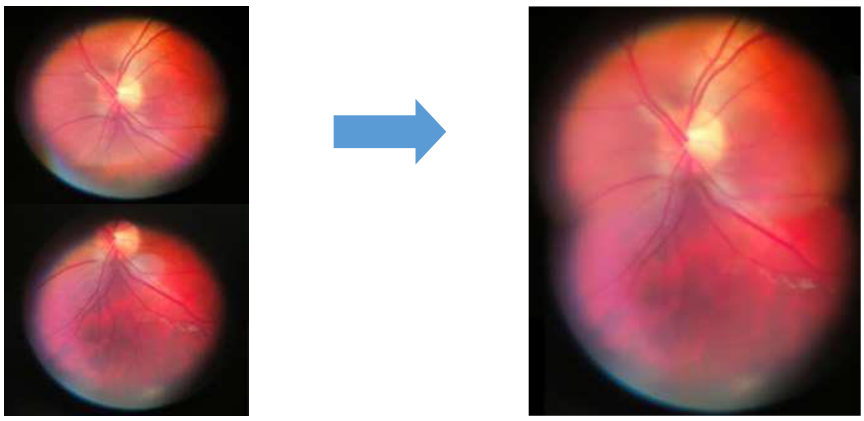

Figure 4.20: Stitching. Two images are put together, by recognition of similar points.

To simulate internal fixation points in BEAM IV, there is the need to simulate another different path that can be called Display Path. The only requirement for this path is that the rays are focused as near the retina as possible. The focusing doesn't need to be as perfect as for the imaging path, because the patient only needs to have a target to look for, so even if the target is blurred the patient will still fairly know where to be staring. To do it another PCX lens and another light source are used as well as another beamsplitter to separate this path from the illumination path. In Figure 4.21 is demonstrated the display path for one internal fixation point centered with the optical path.

To check the feasibility of a different pupil alignment, a model similar to the one used for the single fixation point at the center was used. The main difference is that the light source isn't centered with the optical path.

After searching on the market for an available Matrix of LED's that could be small enough to fit inside the prototype, a red light 8x8 matrix with 20 mm size square and manufactured by Adafruit, was chosen. After studying the datasheet, available in the website (https://www.adafruit.com/product/454), the LEDs chosen were the 4 central ones for the central fixation point and 4 pairs of two for the periphery fixation points, with each pair being at a 6.25 mm distance from the center at each direction. The diagram of Figure 4.22 helps in the understanding of different the LEDs chosen.

Only one of the deviated fixation points needs to be simulated, because, being the

optical system roundly symmetrical, all rays equally deviated from the center will show the exact same behavior. The simulation results are shown in Figure 4.23 and show the rays being focused 15° away from the center.

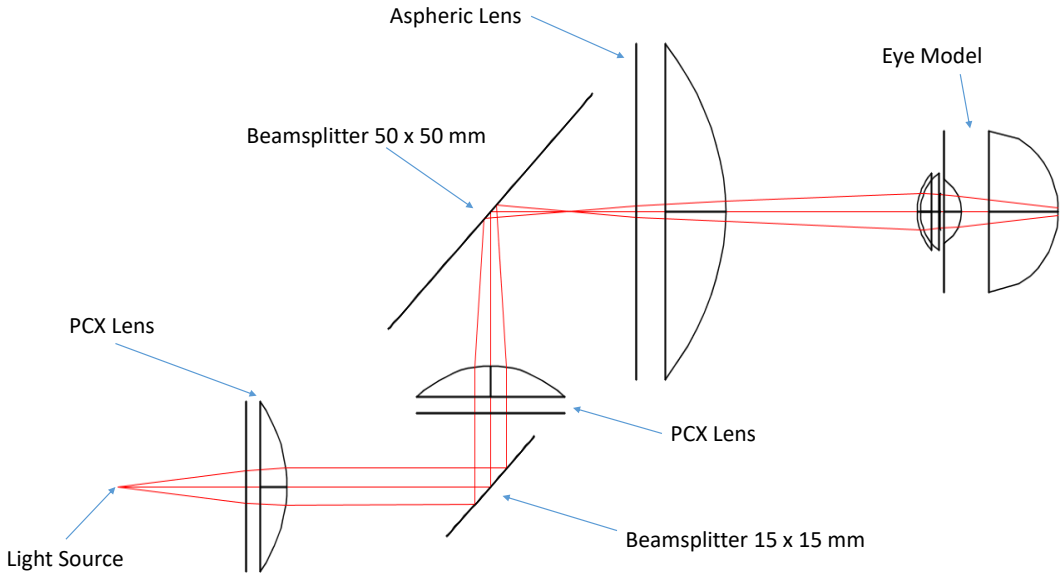

Figure 4.21: Centered Internal Fixation Point being focused on the Retina.

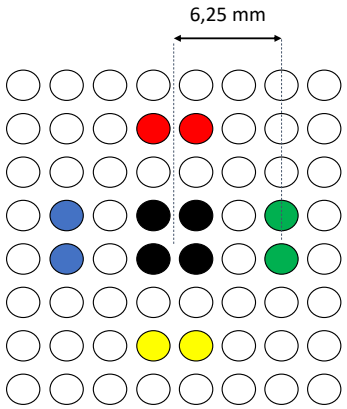

Figure 4.22: Representation of the LED's that will be turned on for different Pupil alignments. The black dots represent the LEDs that will be turned on for the central fixation point and the colored pairs will be on, each at a time to see the periphery. Only the distance between the center and the pair of LED's on the right is described but it is the same for any of the different directions.

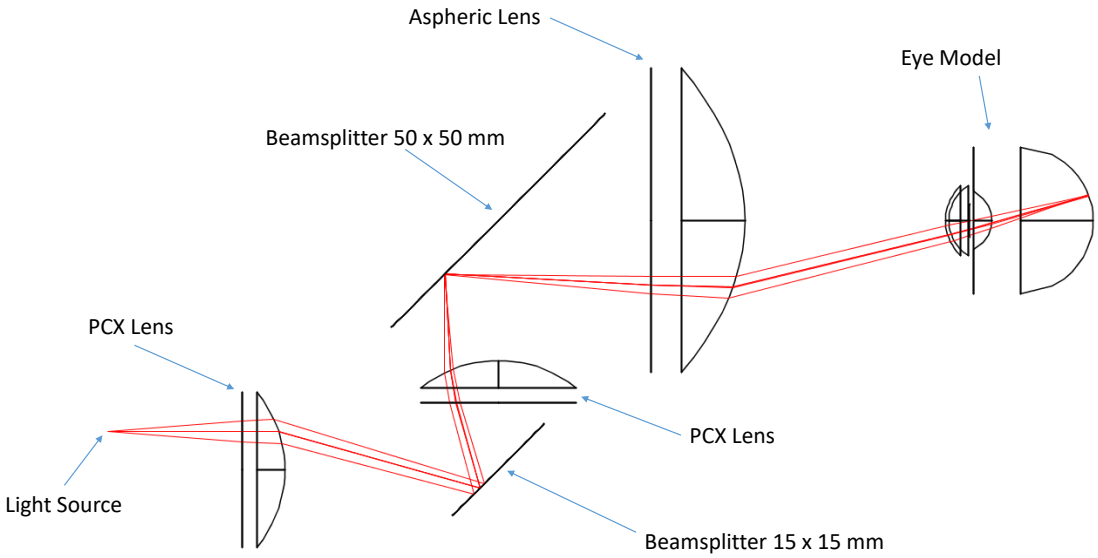

Figure 4.23: Internal Fixation points simulation for the matrix available in the market described in Figure 4.22, considering a light source 6.25 mm off-axis with the rays being focused 15 degrees away from the center.

Chapter 5

Mechanical Prototyping

The optical system previously described is to be implemented in a 3D printed prototype. The design of the mechanical prototype was developed using Solid Works Student Version 2016, a really easy-to-use software with several toolboxes making the design more realistic. A previous prototype had already been developed by Fraunhofer but not compatible with the optical system described in chapter 4. The previous prototype can be seen in Figure 5.1.

Figure 5.1: Image of the previous prototype developed by Fraunhofer Portugal AICOS.

The prototype to be designed has the follwoing main goals :

- Ergonomic use for the examiner and comfortable for the patient.

- Small enough to be easily transported.
- Placement of the lens precisely according to the optical system described in section 4.6.
- Smartphone support that ensures that the camera is centered with the optical path.
- Precise adjustment of the Objective lens to be used in patients with Refractive Errors(+5 to -5 mm).

The shape of the previous prototype was maintained as it was considered substantially ergonomic. The lens placement and casing was renewed as the distances between lenses for the new optical system were completely different from the previous ones, leading to a much smaller prototype as can be seen in Figure 5.2. The size of the prototype can be estimated by comparison with the size of the smartphone. The smartphone support was also based in a previously developed prototype and got the perfect capabilities for a LG Nexus 5X, at the same time that ensured the centering of the smartphone camera with the optical path. The most difficult feature to be achieved was the precise movement of the objective lens. The movement not only needed to be precise, but also needed to allow a continuous adjustment allowing the examiner to search for the most focused image of the retina, thus granting the best possible focusing of the retina. Was accomplished using a rack and pinion model, with M5 threads. The use of a Rack and Pinion mate can help the examiner to perfectly search for the best possible working distance.

Figure 5.2: Mechanical prototype designed using Solid Works in red with the rack and pinion assembly in gray and the smartphone in black.

The bolts and nuts needed to support the system were designed according to ISO normalization having M5 size so, due to its low cost and availability on the market, are

expected to be bought[1,2]. The rack and the pinion as a result of its higher price, at first, are expected to be 3D printed, for testing.

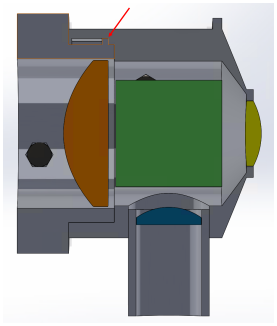

a Configuration for Myopic Eyes 4.16.

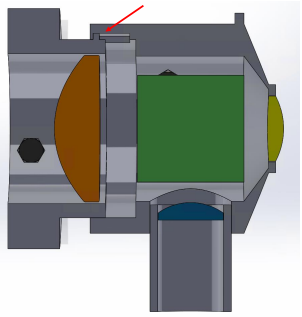

b Configuration for Hyperopic Eyes 4.17.

Figure 5.3: Section view of the prototype. In blue is the PCX Condenser Lens, in yellow the Best-Form Lens, in orange the Aspheric Lens and in green the Beamsplitter. The Beamsplitter is in the form of a cube only for simulation, to simplify the fixation in the mechanical case. The small piece highlighted by the red arrow limits the adjustment between the aspheric lens and the beamsplitter.

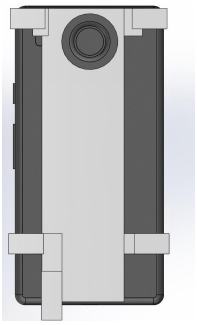

a View from the rear part of the smartphone.

b View from the front part of the smartphone.

Figure 5.4: Support attached to the smartphone. Is visible that the smartphone camera is centered with the prototype which is in its turn centered with the optical path. The support is ideally designed for the LG Nexus 5X, but allows adjustments.

Other solution to allow the movement of the lens would be by the use of threaded surfaces in both sides, so the rotation of the objective ensures a change in the working distance. This approach was rejected because it is expected the future implementation of a piece leaning against the patient forehead, to guarantee the centering of the eye with the optical path. The rotation of this piece, in contact with the patient, would not be comfortable or, possibly, safe. Other reason for the discarding of the threaded surfaces was the possibility of using crossed polarizers, in the future.

[1] Bolts availabe on - https://www.fabory.com/pt/fixacao/parafusos-sextavado-exterior/parafuso-cabeca-sextavada-iso-4014-aco-direita-sem-tratamento-de-superficie-8-8-m5x25/p/01000050025

[2] Nuts available on - https://www.fabory.com/pt/fixacao/porcas-porcas-de-rebitar-insertos/porca-sextavada-iso-4032-aco-direita-sem-tratamento-de-superficie-10-m5/p/04124050001

The mechanical prototype here developed doesn't contemplate the matrix of LED's and the other optical components needed for the implementation of the internal fixation points because it is intended the evaluation of the fundamental optical path (illumination and imaging paths), described in sections 4.3 and 4.4 before the implementation of internal fixation points.

Chapter 6

Light Hazard Measurement

Besides the design of a fundus camera prototype, light hazard measurements were performed on the previous prototype (Figure 2.12). The tests regarded ISO 15004-2 [4] and ISO 10940 [5] norms, being the first for light hazard protection of Ophthalmologic Instruments and the second specifically for Fundus Cameras. These measurements are mandatory, in this kind of instruments, in order to check the safety of eye examinations.

The illumination is performed in a way that during the visualization (search for the correct spot to be imaged) the intensity of the light is lower and during the acquisition the intensity is higher in order to improve the quality of the image to be saved. Two different LEDs, one that emits visible light and another one emitting NIR light are used. The intensity of the light source is controlled using Pulse-Width Modulation (PWM) (explained in the annex III).

The intensity of the emitted light by each LED is changeable through a smartphone application presented in Figure 6.1. After the connection with the prototype, the user can continuously change the intensity level for each LED at a time.

6.1 Power Measurements

The white light LED emits at several different wavelengths and the NIR Spectrum only has one peak, leading to different testing procedures, one for each LED and another for the Acquisition Mode :

- NIR LED :
  - Emission Spectrum measurement with a spectrometer to check the wavelength of the peak.

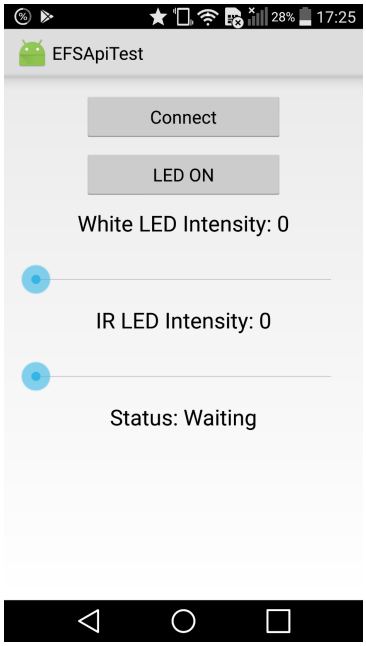

Figure 6.1: The intensity control of the LED is performed with a smartphone application called EFSApiTest, previously developed by Fraunhofer that allows a continuous change between several levels of emission intensity.

  - Power measurement with a photodiode power sensor at the previously discovered wavelength.

- Visible LED :

  - Emission spectrum measurement with a spectrometer to check the wavelength of each peak.
  - Power measurement with a photodiode power sensor at the previously discovered wavelengths.

- Acquisition Mode :

  - Voltage and time lapse measurement using a photodiode and an oscilloscope.

The setups used for the measurements are presented in the annex IV.

For the spectrum calculation, an Edmund Optics, neutral density optical filter [50] with about 20% transmittance was placed between the prototype and the optical fiber, to prevent spectrometer saturation.

An algorithm developed in python was used so, the information obtained from the spectrums could be processed. The data that must be extracted from the spectrums are the wavelength of the peaks, the area beneath each peak and the maximum number of counts for each peak wavelength. The code for the algorithm is available in the annex VI and the results are presented in the annexes VII and VIII.

6.1.1 Near Infra-Red LED

For the NIR LED, the power values obtained directly with the photodiode power sensor are in the table 6.1.

Table 6.1: Near Infra-Red LED measurements

Wavelength(nm) / Smartphone Level	820	836
5	0,1345 mW	
15	0,35 mW	
30	0,660 mW	
255		3,48 mW

As it can be noticed in the table, for the more intense configuration the emission wavelength was increased by 16 nm, this can be explained by the decrease on the energy gap between energy levels that every semiconductor suffers with the increase of the temperature [51, 52]. The energy gap is inversely proportionally related with the wavelength and the relation can be described with the equation 6.1.

$$E_g = \frac{hc}{\lambda} \tag{6.1}$$

So, for the NIR LED when the smartphone level increases there is an increment in the current reaching the LED and thereafter the temperature rises. With the increase in temperature, the energy gap is reduced and the wavelength is increased.

6.1.2 Visible LED

For the visible LED to reach the final value on the emitted power, more measurements are needed. With the observation of the Spectrum (observable in the annex VII) it was understood that the LED to emit white light, had peaks at two different wavelengths, one at 565 nm (yellow region of the electromagnetic spectrum) and another at 464 nm (blue region of the electromagnetic spectrum). Firstly, the values were obtained with the photodiode power sensor at both wavelengths leading to the table 6.2.

Table 6.2: White LED measurements

Wavelength(nm) / Smartphone Level	**464**	**565**
5	0,077 mW	0,0893 mW
30	0,280 mW	0,330 mW
100	0,478 mW	0,565 mW
255	0,615mW	0,732 mW

As the visible LED is a broadband emitter and the photodiode responsivity depends on the wavelength, the values for the visible LED can't be measured directly and the spectrums must be used to check the value for each peak.

The procedure to acquire the final values from the power measurements and the spectrum obtained was as following :

- Calculate the maximum number of counts for each peak on the spectrum.
- Calculate the mean power using the equation 6.2.

$$M_P = \frac{P_{yellow} \times C_{yellow} + P_{blue} \times C_{blue}}{C_{blue} + C_{yellow}} \tag{6.2}$$

  Where M_P is the mean power of the LED, P_{yellow} and P_{blue}, are the powers measured with the radiometer and C_{yellow} and C_{blue}, are the number of counts in the peak for the spectrum, at 565 nm and 464 nm respectively.

- Using a Gaussian Fit function from NumPy library, integrate the Area beneath each peak.
- From the values obtained calculate the proportion of each peak on the total spectrum area.
- Calculate the power at each wavelength using the equation 6.3.

$$\begin{aligned} P_{peak1} &= A_{blue} \times M_P \\ P_{peak2} &= A_{yellow} \times M_P \end{aligned} \tag{6.3}$$

  Where P_{peak1} is the approximated emission power at 464 nm, P_{peak2} is the approximated emission power at 565 nm, A_{blue} and A_{yellow} are the relationship between the area of the respective peaks and the total area of the spectrum.

It is important to explain that this procedure is an approximation, but by having in account the optical power measurements and both the counts and the area in the spectrum, can lead to a very approximated value. As an example will be demonstrated the calculus of the power values with the smartphone app at level 255 for the visible LED.

The accuracy of the Gaussian Fit can be evaluated in the spectrums obtained in the annex VII.

The values obtained from the power tables and from the python output file VIII are :

- P_{yellow} - 0.732 mW
- P_{blue} - 0.615 mW
- C_{yellow} - 5040.58
- C_{blue} - 53599.80

- $A_{yellow}(\%)$ -27.22%
- $A_{blue}(\%)$ -72.78%

To get the mean power it is needed to use the equation 6.2.

$$\begin{aligned} M_P &= \frac{P_{yellow} \times C_{yellow} + P_{blue} \times C_{blue}}{C_{blue} + C_{yellow}} \\ M_P &= \frac{0.732 \times 5040.58 + 0.615 \times 53599.8}{53599.8 + 5040.58} \\ M_P &= 0.625 \text{ mW} \end{aligned} \tag{6.4}$$

To understand the power at each wavelength, the equations in 6.5 were used :

$$\begin{aligned} P_{peak1} &= A_{blue} \times M_P & P_{peak2} &= A_{yellow} \times M_P \\ P_{peak1} &= 0.7278 \times 0.625 & P_{peak2} &= 0.2722 \times 0.625 \\ P_{peak1} &= 0.455 \text{ mW} & P_{peak2} &= 0.170 \text{ mW} \end{aligned} \tag{6.5}$$

After repeating the previous process for all the desired smartphone levels, the values obtained are presented in the table 6.3

Table 6.3: White LED measurements

Wavelength(nm) / Smartphone Level	464	565
5	0,024 mW	0,058 mW
30	0,092 mW	0,208 mW
100	0,239 mW	0,259 mW
255	0,455mW	0,170 mW

It is noticeable, by the table 6.3 and by the spectrums, that for the visible LED as the current supplied increases the blue wavelength gets more representative occurring also a shift on the blue peak towards higher wavelengths. With the yellow wavelength occurs the opposite. The first can be caused by the increase in current and the second can be provoked by an increase in the junction temperature [53].

6.1.3 Acquisition Mode

In the Acquisition Mode the LED emits more intense visible light during a shorter time.

When the acquisition mode is used, has can be seen in Figure 6.2, there is, not only the voltage variation caused by the flash, but also the voltage variation caused by the previously selected level in the EFSApiTest. The voltage and the emitted power are proportional, so to know the power emitted at the acquisition mode it was helpful to use an already known value for the smartphone level. The value chosen was 30 on the

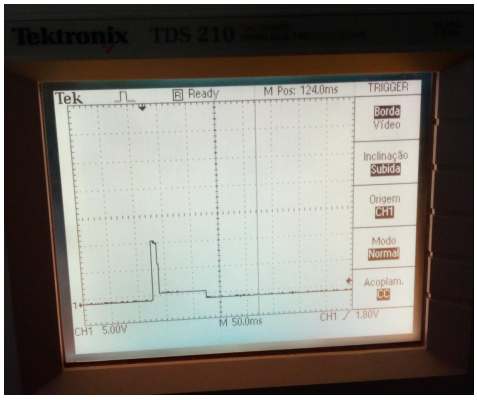

Figure 6.2: Oscilloscope display, presenting the voltage change detected when the acquisition mode is used. The peak is caused by the flash and the lower step is the voltage caused by the LED at level 30 in the smartphone App.

smartphone level, considered to be adequate for visualization of the fundus. Considering the direct proportionality between both values, the power for the Flash was discovered. The voltage variation for the 30 smartphone level corresponding to the smaller step in Figure 6.2 was 1.5 V as for the flash was 11 V.

As for a voltage output of 1.5 V the smartphone level will be 30, than for a voltage output of 11 V the theoretical smartphone level would be 220. Using again rules of 3. If for a 30 smartphone level, 565 nm power is 0.208 mW (Table 6.3), then for a 220 smartphone level is 1.53 mW. For the 464 nm wavelength, using an analogous procedure, the emitted power during the flash is 0.67 mW.

6.2 ISO Results

As the limit values provided on the ISO Norms are presented in irradiance, the retinal area must be calculated. One way to calculate it is by using the formula on the equations 6.6 and 6.7 [5].

$$\omega = 4\pi \sin^2\left(\frac{\alpha}{4}\right) \tag{6.6}$$

$$A = (1.7\text{cm})^2 \times \omega \tag{6.7}$$

Where ω is the illumination solid angle in steradians, α is the full cone angle in degrees and A is the retinal area illuminated in square centimeters. Considering a Field of View of 40° the solid angle is 0.3789 sr and consequently the retinal area is 1.095 cm^2.

The measurements for both LEDs were performed at the maximum intensity setup (255 smartphone level) and will be described in the following subsections.

6.2.1 Near Infra-Red LED

Before testing if the measured values reach the acceptable limits, the calculus of several variables and coefficients must be performed. For the NIR LED the variables are :

- Power - 3.48 mW
- $R(\lambda)$ - 0.536
- Irradiance - 3.178 mW/cm^2

Where $R(\lambda)$ is the thermal hazard weighting function and the irradiance is obtained by the quotient between the power and the retinal area. For wavelengths superior to 780 nm there is no aphakic photochemical hazard weighting function, so the value of $A(\lambda)$ is 0 and only the retinal thermal hazard must be calculated.

- 5.4.1.6- **Retinal visible and infrared radiation thermal hazard**

$$E_{VIR-R} = \sum_{380}^{1400} E_\lambda \times R(\lambda) \times \Delta\lambda \tag{6.8}$$

As,

$$E_\lambda = \frac{\Phi(\lambda)}{dA \times d\lambda} \tag{6.9}$$

The calculation on the $\Delta\lambda$ is not needed.

$$\begin{aligned} E_{VIR-R} &= \sum_{380}^{1400} \frac{\Phi(\lambda)}{dA \times \Delta\lambda} \times R(\lambda) \times \Delta\lambda \\ E_{VIR-R} &= \sum_{380}^{1400} \frac{\Phi(\lambda)}{dA} \times R(\lambda) \\ E_{VIR-R} &= \sum_{380}^{1400} E \times R(\lambda) \\ E_{VIR-R} &= 3.178 \times 0.536 \\ E_{VIR-R} &= 1.7 \text{ mW}/cm^2 \end{aligned} \tag{6.10}$$

6.2.2 Visible LED

As in the previous section, the calculus of several variables must be performed. For the two different wavelengths, this variables have different values, being :

- 464 nm
  - Power - 0.455 mW
  - A(λ) - 0.72
  - R(λ) - 1
  - Irradiance - 0.4155 mW/cm^2
- 565 nm
  - Power - 0.170 mW
  - A(λ) - 0.005
  - R(λ) - 1
  - Irradiance(E) - 0.155 mW/cm^2

Where $A(\lambda)$ is the aphakic photochemical hazard weighting function, $R(\lambda)$ is the thermal hazard weighting function and the irradiance is obtained by the division between the power and the retinal area. The values that must be calculated are presented in the next section.

- 5.4.1.3- **Retinal photochemical aphakic light hazard**

$$E_{A-R} = \sum_{350}^{700} E_\lambda \times A(\lambda) \times \Delta\lambda \tag{6.11}$$

Using once again the equation eq. (6.9)

$$\begin{aligned} E_{A-R} &= \sum_{350}^{700} \frac{\Phi(\lambda)}{dA} \times A(\lambda) \\ E_{A-R} &= \sum_{350}^{700} E \times A(\lambda) \\ E_{A-R} &= 0.4155 \times 0.72 + 0.155 \times 0.005 \\ E_{A-R} &= 0.299 + 0.000776 \\ E_{A-R} &= 0.2998 \text{ mW}/cm^2 \end{aligned} \tag{6.12}$$

- 5.4.1.6- **Retinal visible and infrared radiation thermal hazard**

$$E_{VIR-R} = \sum_{380}^{1400} E_\lambda \times R(\lambda) \times \Delta\lambda \tag{6.13}$$

$$\begin{aligned} E_{VIR-R} &= \sum_{380}^{1400} \frac{\Phi(\lambda)}{dA \times \Delta\lambda} \times R(\lambda) \times \Delta\lambda \\ E_{VIR-R} &= \sum_{380}^{1400} \frac{\Phi(\lambda)}{dA} \times R(\lambda) \\ E_{VIR-R} &= \sum_{380}^{1400} E \times R(\lambda) \\ E_{VIR-R} &= 0.4155 \times 1 + 0.155 \times 1 \\ E_{VIR-R} &= 0.571 \text{ mW}/cm^2 \end{aligned} \tag{6.14}$$

6.2.3 Acquisition Mode

For the acquisition mode, after the measurements previously described there is the need to calculate the weighted retinal visible and infrared radiation radiant exposure, $H_{VIR\text{-}R}$. The variables needed for this calculation are the following :

- Nominal pulse duration (Δt) - 0.015 s
- Energy Integration time (t) - 0.015 s
- 464 nm :
  - Power - 0.67 mW
  - R(λ) - 1
  - Irradiance - 0.611 mW/cm^2
- 565 nm :
  - Power - 1.53 mW
  - R(λ) - 1
  - Irradiance(E) - 1.397 mW/cm^2

The nominal pulse duration is determined by the time lapse equal to the full width of the pulse at half maximum of the pulse. The energy integration time is the full pulse width for an individual pulse. The value attributed to each one was the same because it is difficult to understand the differences between the full width at half maximum and the full pulse width for an individual pulse. This condition doesn't invalidate the following measurements because an higher value for the nominal pulse duration will increase the

weighted retinal visible and infrared radiation radiant exposure limit. And if a bigger Δt is considered and the result is still below the limit, the real value would also surpass the test.

- 5.4.2.1- **Weighted retinal visible and infrared radiation radiant exposure**

$$H_{VIR-R} = \sum_{380}^{1400} (E_\lambda \times \Delta t) \times R(\lambda) \times \Delta\lambda \tag{6.15}$$

$$H_{VIR-R} = \sum_{380}^{1400} \left(\frac{\Phi(\lambda)}{dA} \times \Delta t \right) \times R(\lambda)$$

$$H_{VIR-R} = \sum_{380}^{1400} E \times \Delta t \times R(\lambda) \tag{6.16}$$

$$H_{VIR-R} = 0.532 \times 0.015 \times 1 + 1.201 \times 0.015 \times 1$$

$$H_{VIR-R} = 0.0301 \text{ mJ}/cm^2$$

6.3 ISO Norms Compliance

To understand if medical tests can be performed the values calculated in the previous sections must be compared with the limits described in the ISO Norms. First it will be revised if the prototype can be classified as Group 1 Instrument. In table 6.4 it is presented a comparison between the calculated values and the ISO limits.

Table 6.4: ISO Norms Compliance

Mode	Hazard	Result	Limit	Comment
Visible LED	Retinal Photochemical Aphakic Light Hazard	0.2998 mW/cm^2	0.220 mW/cm^2	Above the limit
	Retinal Visible and Infrared Radiation Thermal Hazard	0.571 mW/cm^2	700 mW/cm^2	Below the limit
Near Infra-Red LED	Retinal Visible and Infrared Radiation Thermal Hazard	1.7 mW/cm^2	700 mW/cm^2	Below the limit
Acquisition	Weighted Retinal Visible and Infrared Radiation Radiant Exposure	0.0301 mJ/cm^2	$6t^{\frac{3}{4}} = 257$ mJ/cm^2	Below the limit

As the result for the Retinal Photochemical Aphakic Light Hazard is above the Group 1 Instrument limit, the Group 2 instrument correspondent measurement must be performed. The parameter for Group 2 instruments is the Weighted Retinal Radiant Exposure. For the calculus of exposure values on continuous wave instruments, as described in the ISO norm for Fundus Cameras [5], the value for the time is 7200 seconds. In the equation 6.18 is presented the calculus for this hazard.

- 5.5.1.6- **Weighted retinal radiant exposure**

$$H_{A-R} = \sum_{305}^{700} (E_\lambda \times t) \times A(\lambda) \times \Delta\lambda \tag{6.17}$$

$$\begin{aligned} H_{A-R} &= \sum_{305}^{700} E \times t \times A(\lambda) \\ H_{A-R} &= 0.4155 \times 7200 \times 0.72 + 0.155 \times 7200 \times 0.005 \\ H_{A-R} &= 2158 \text{ mJ}/cm^2 = 2.158 \text{ J}/cm^2 \end{aligned} \tag{6.18}$$

For this parameter, the limit is 10J/cm^2. To determine the time needed to reach a potential optical radiation hazard for aphakic retinal exposure, the previous equation can be solved in order to t. The calculus is presented in the equation 6.20.

- 5.5.1.6- **Weighted retinal radiant exposure (in order to t)**

$$H_{A-R} = \sum_{305}^{700} (E_\lambda \times t) \times A(\lambda) \times \Delta\lambda \tag{6.19}$$

$$\begin{aligned} H_{A-R} &= \sum_{305}^{700} (E_\lambda \times t) \times A(\lambda) \times \Delta\lambda \\ H_{A-R} &= \sum_{305}^{700} E \times t \times A(\lambda) \\ 10000 &= 0.4155 \times t \times 0.72 + 0.155 \times t \times 0.005 \\ 10000 &= 0.299 \times t + 0.000776 \times t \\ 10000 &= 0.299977 \times t \\ t &= \frac{10000}{0.299977} \\ t &= 33358s \end{aligned} \tag{6.20}$$

So, it can be concluded that to reach the guideline for Group 2 Instruments on weighted retinal radiant exposure the prototype must be on for 33358 s (about 9 hours). The instrument can then be regarded as a Group 2 Instrument.

The photodiode power sensor used was a PD300 supplied by Ophir and the spectrometer was a Avaspect 2048 (360 – 1100 nm) supplied by Avantes.

Chapter 7

Imaging Path Practical Results

The capabilities of the Imaging Path using the components previously described in the section 4.4 were tested [1]. The following list presents the used materials as well as the suppliers:

- Optical Table;
- Optical Post Holders, ThorLabs and Edmund Optics;
- S-LAH64 CNC-Polished Aspheric Lens, 40.0 mm Focal Length, 50 mm ϕ, ThorLabs;
- N-BK7 Best-Form Lens, 40 mm Focal Length, 25.4 mm ϕ, Thorlabs
- Microsoft Lumia 360;
- N-BK7 Plano-Convex Lens, 38.1 mm Focal Length, 25.4 mm ϕ, VIS-NIR Coated, Edmund Optics;
- Adjustable Iris;
- Graph paper;
- Black Cardboard.

The Optical Post Holders were used to allow the fixation of the components in the Optical Table. The system was tested with a 4 mm iris for simulation of the pupil, placed as near to the 38.1 mm focal length PCX Lens as possible, used to replace the eye refractive center. For simulation of the retina, a graph paper was used to facilitate measurements on the FOV. The graph paper was placed 38 mm to the right of the lens, in order to allow the

[1] The tests were performed at Laboratory of Optics, Lasers and Systems (LOLs) in Lisbon.

best possible focus. The smartphone used to collect the pictures was a Microsoft Lumia 650 with 63.4° horizontal angle of view and 49.7° vertical angle of view, fixed 20 mm to the left of the best-form lens. These tests didn't use any particular light source, only the lights in the room. A black paperboard was placed to cover the optical system, to prevent the entrance of light in the middle of the optical path and undesired reflections. The distances between the components described in the section 4.4, were defined as close as possible to the distances modulated with BEAM IV section 4.4. The Figure 7.1 is a picture taken on the testing setup and Figure 7.2 shows a diagram of the components placement with the distances between them.

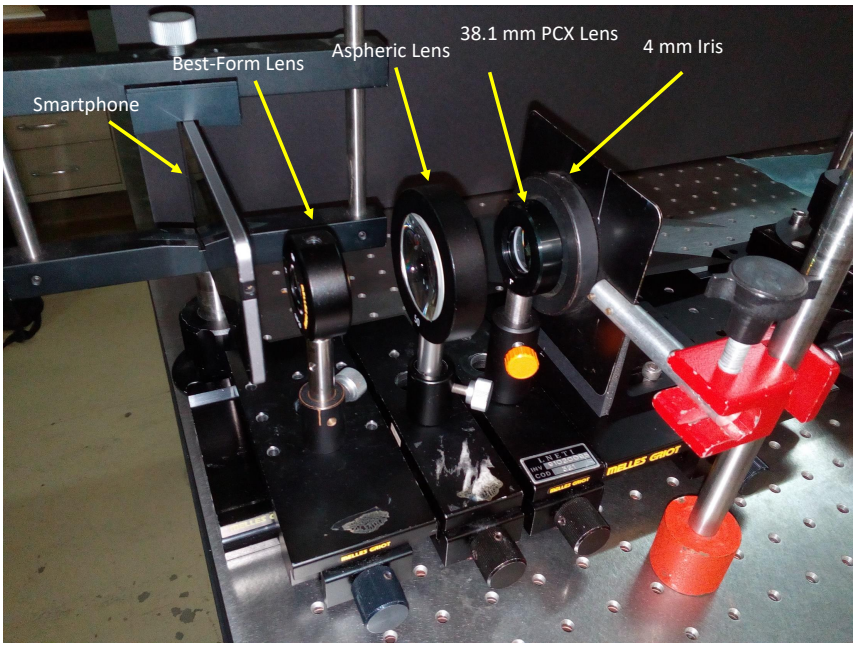

Figure 7.1: Photograph taken on the setup used to perform tests on the Imaging Path. The milimitter paper was covered by the outer piece of the iris.

As the used smartphone as a slightly smaller FOV than the Nexus 5X, to avoid the crop of the image, the placement of the smartphone was expected to be further from the best-form lens. Although, the best focus was accomplished by placing the smartphone closer to the Best-Form. This can be explained by the variability of the smartphone camera optical system, before actually reaching the CMOS Sensor.

Despite all the differences between this testing conditions and the ones presented in the section 4.4, the images obtained (Figure 7.3) showed satisfactory capacities.

The FOV can be calculated by the equation in the annex II. In this case, the equation 7.1 to calculate the half angle is as following :

$$\alpha = \tan^{-1}\left(\frac{X_{distance}}{Z_{distance}}\right) \tag{7.1}$$

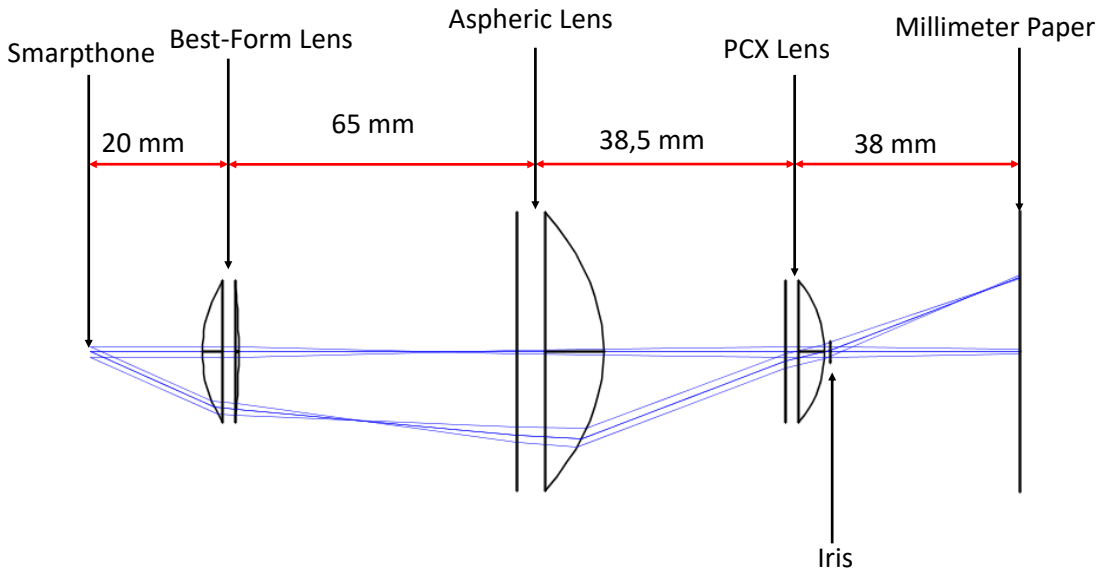

Figure 7.2: Diagram showing the placement of the different components with the distances between them represented. The Iris was placed after the PCX lens as near as possible.

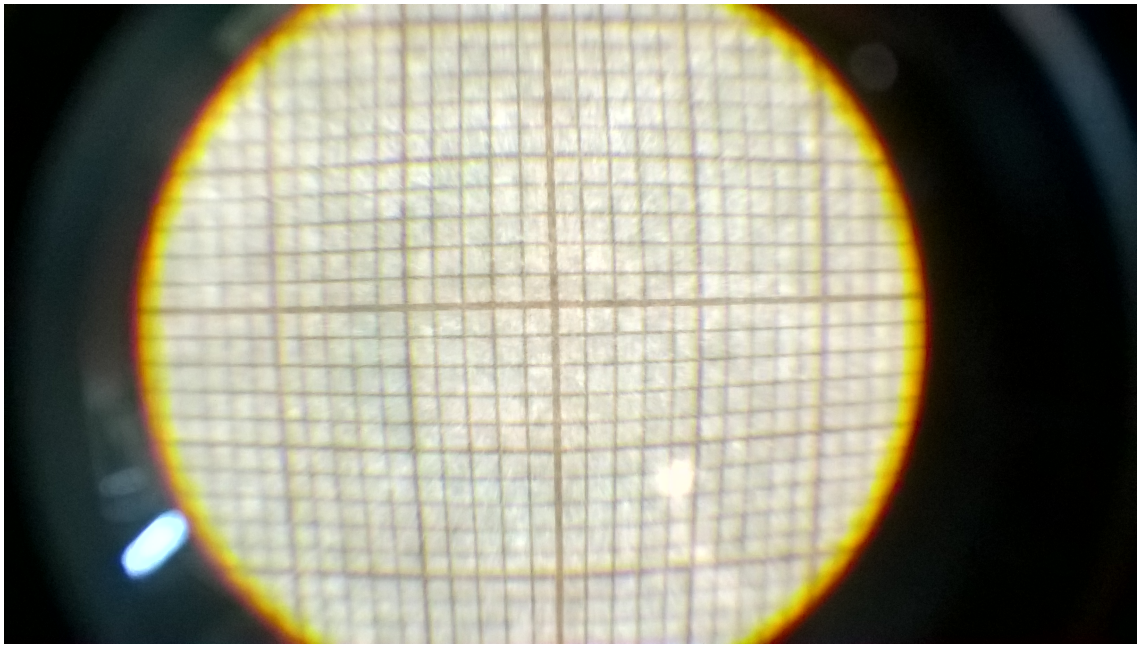

Figure 7.3: Image obtained with Microsoft Lumia 360. It can be seen that 14 mm at each side are observable. The crop existing in the bottom and the top can be justified by the utilization of a smartphone with a smaller Field of View than the Nexus 5X, the idealized smartphone during the BEAM IV simulation. It can be observed qualitatively that the resolution is better on the center than on the periphery.

Where $X_{distance}$ is the distance in any direction, between the center and the circumference limiting the observable area. $Z_{distance}$ is the distance between the refractive center, in this case the PCX Lens and the target, the graph paper. So, the $X_{distance}$ by observation of the Figure 7.3 can be considered to be about 14 mm. Then, the calculated α is about 20.22°, leading to a total field-of-view 40.44 °.

Besides the FOV, the spatial resolution was also assessed. Considering an 8MP resolution camera, the captured picture has 3272×2454 pixels. As the horizontal resolution is superior, the calculations are presented for the vertical resolution. Due to the crop in the vertical field-of-view, the vertical half-angle of view will be of about 17.5°, corresponding to 6.0 mm in the retina (according to BEAM IV simulations). Thus, the spatial resolution is 4.9 μm, meaning that each pixel contains 4.9 μm of the retinal area, which is sufficient to observe the expected smallest microaneurysms (25 μm).

Still based in the previous calculus, the usage of a smartphone camera, instead of a higher resolution camera, is justified by the eye diffraction limit. The eye diffraction limit is directly related with the patient eye pupil and can be assessed by the eqs. (7.2) and (7.3) [54].

$$NA = n \times \sin(\theta) = n \times sin\left(\arctan\left(\frac{D}{2 \times f}\right)\right) \tag{7.2}$$

Where NA is the Numerical Aperture of the eye, n is the index of refraction of the media in which the light is focused, θ is the half angle of the focused beam at the sample, D is the entrance pupil diameter (beam size) and f is the focal length [54]. Knowing the Numerical Aperture is possible to obtain the resolution by the following equation.

$$R = \frac{\lambda}{2 \times NA} \tag{7.3}$$

Where R is the Resolution, λ is the wavelength of the light and NA is the Numerical Aperture [54].

Doing the calculus, for a 5 mm pupil eye receiving light of about 500 nm, the NA is 0.167 and the diffraction limit is 1.5 μm. As this value is close to the resolution of the system and counting with the existence of other eye resolution limiting features (aberrations) besides the diffraction limit [54], a sensor with a much higher resolution would be more expensive and the spatial resolution would start to be close to the eye limits.

For aberrations the system can't be measured quantitatively but only qualitatively. This system using only light from the room and not using any specific light source demonstrated an almost aberration free system with more resolution on the center than in the periphery. It is also important to explain that using a plane surface as goal causes more aberrations in the periphery. As the system was design to a curved goal surface (the retina), the focusing in the periphery will be much better in a curved surface than in a

plane surface. The importance of the utilization of an inner prototype surface that absorbs light, avoiding undesired reflections was also addressed with the Figures 7.4 and 7.5, obtained with and without cardboard covering the components respectively. The image without the cardboard is darker when compared with 7.4 and there are more undesired reflections.

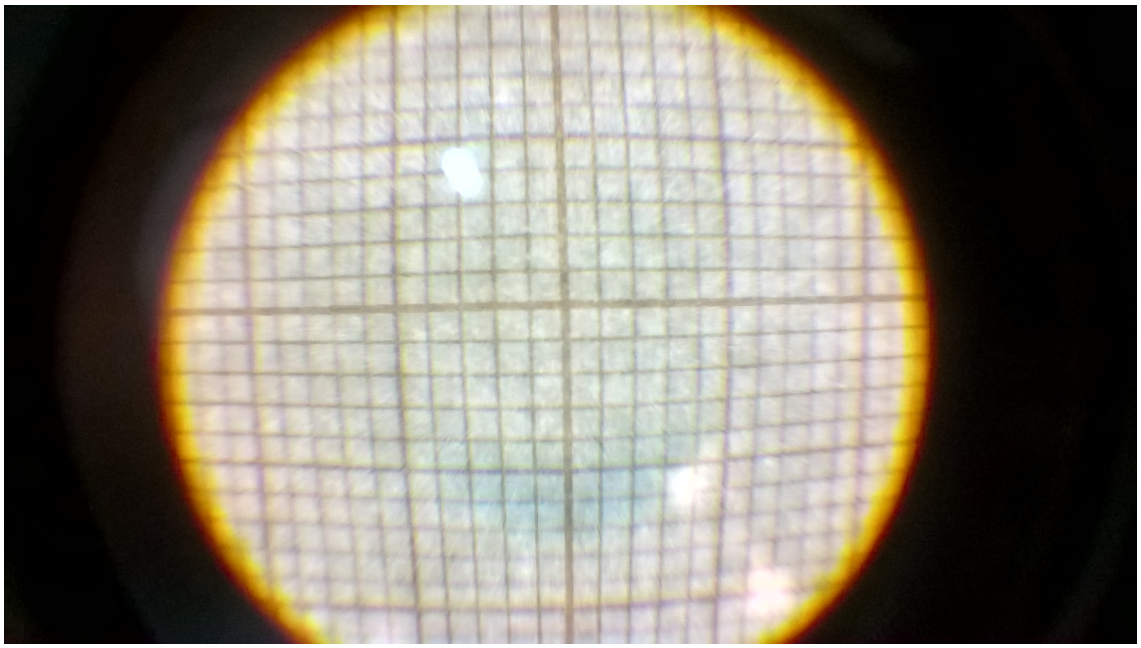

Figure 7.4: Image obtained for the normal eye at focus with black cardboard covering the optical path.

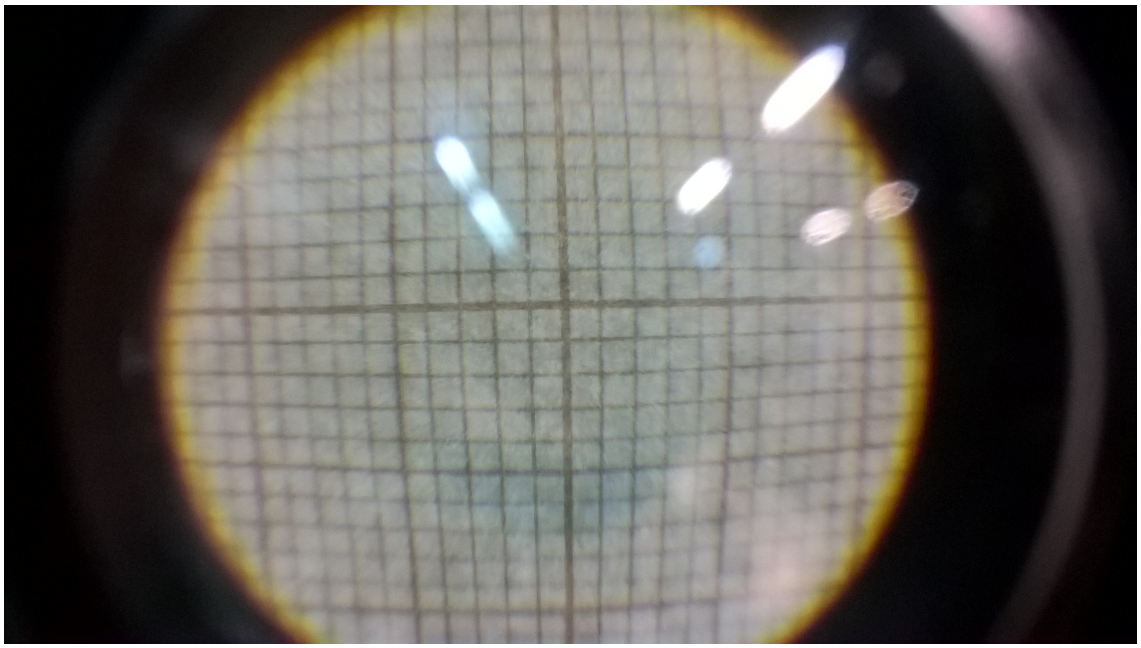

Figure 7.5: Image obtained for the normal eye at focus without black cardboard covering the optical path.

7.1 Imaging Path Practical Tests for Refractive Errors

Other important factor considered was the adjustment of the optical system for eyes with refractive errors. As in the section 4.5, myopia and hyperopia were simulated by moving away and approximating the target about 3 mm (graph paper). The focus was accomplished only by moving away or approximating the aspheric lens about 5 mm. The results are demonstrated on Figures 7.6, 7.7 and 7.8.

The crop existing in the bottom and in the top can be justified by the utilization of a smartphone with a smaller Field of View than the Nexus 5X, the idealized smartphone during the BEAM IV simulation. For all the images the resolution is better on the center than on the periphery.

Performing the same calculations as for the Normal Eye the FOV for the Myopic Eye is 43 ° and for the Hyperopic Eye is 35 °. The existence of such differences is caused by the difficulties to reach a precise placement of the aspheric lens with the used setup.

In the image for the myopic eye the small darker area is caused by the placement of the iris. Ideally, the iris should be placed inside the eye refractive center has occurs with the pupil in a real human eye, placed between the cornea and the crystalline lens. Obviously, it is expected that when the prototype is used in real patients, this problem is eliminated.

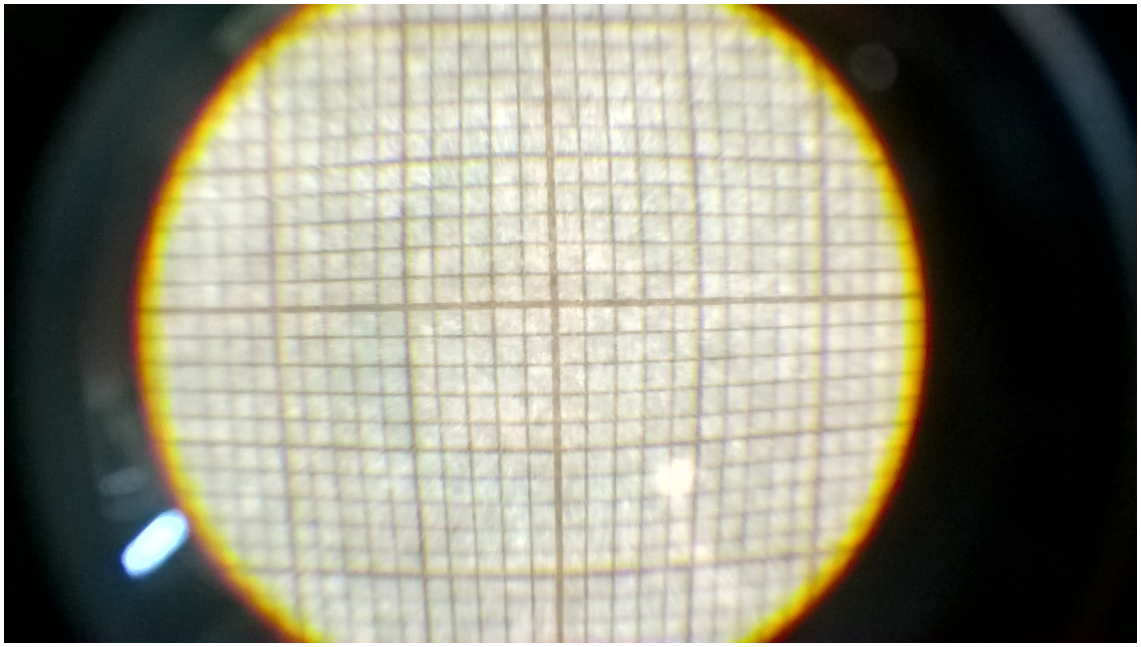

Figure 7.6: Image obtained for a simulated normal eye.

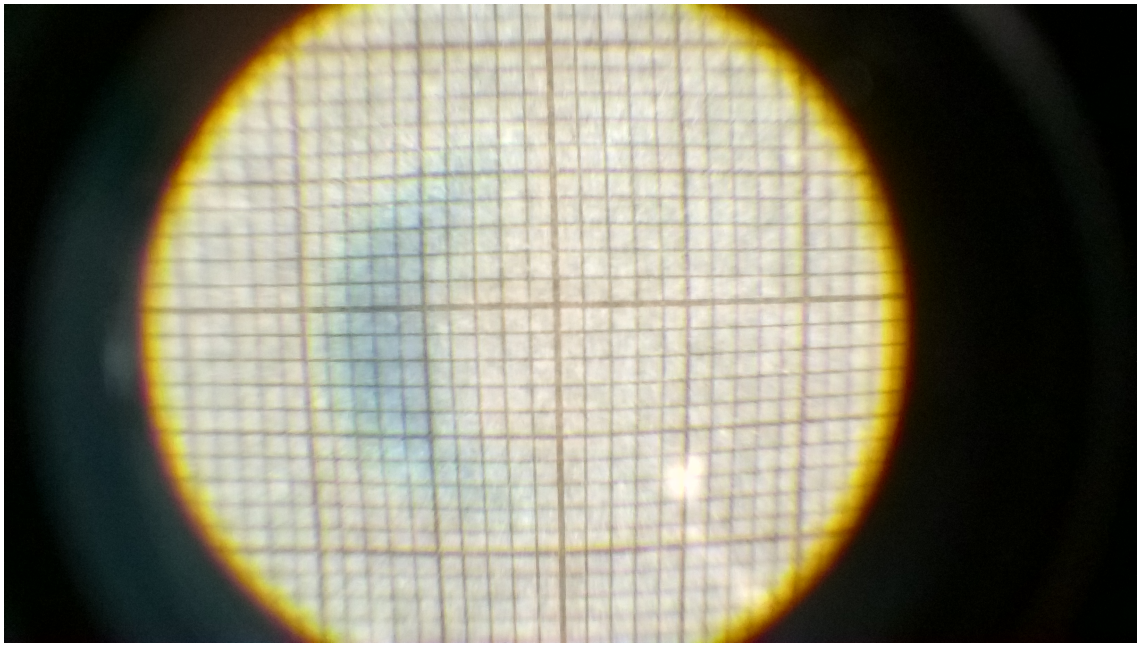

Figure 7.7: Image obtained for a simulated myopic eye. It can be seen that the Field of View increased comparing to the normal eye.

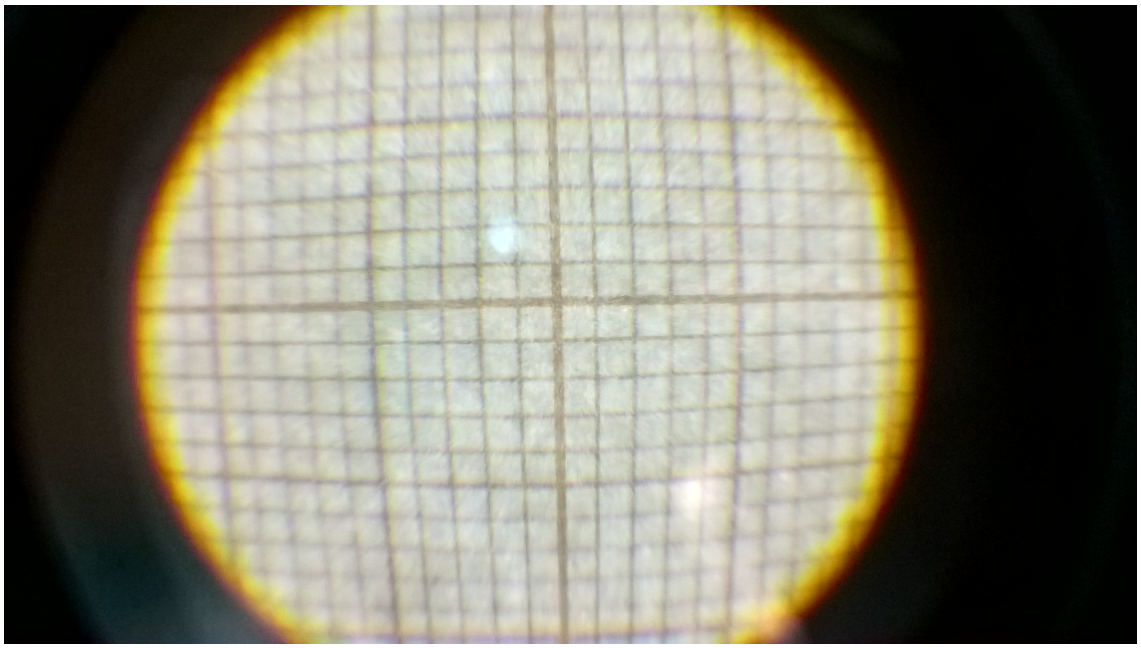

Figure 7.8: Image obtained for a simulated hyperopic eye. It can be seen that the Field of View has diminished when compared with the normal eye.

Chapter 8

Conclusion

Diabetic Retinopathy is the leading cause of blindness in working age adults, affecting 76% of the diabetic patients for more than 20 years, being . Despite the current high awareness on the importance of regular consultation, only achieved by eye examinations, many patients don't have the possibility to perform a frequent follow-up. The prototype designed in this work is expected to be a reliable tool in the diagnose, facilitating high coverage screening and diminishing the burden of screening actions on healthcare systems world-wide.

In this work, an handheld fundus camera prototype was designed and light hazard measurements in a previously developed prototype were performed. In order to improve it, three objectives were set :

- Design of a compact optical system for fundus photography with no need of pupil dilation, ensuring 40º field-of-view with a uniform illumination in all the desired area, comprising several pupil alignments;
- Design of a 3D-printed mechanical prototype for support of the optical system, ensuring transportation and handheld screening;
- Light Hazard measurements on a previously developed fundus camera prototype.

A compact optical system with the capabilities described above was actually designed, being able to detect the smallest lesions associated with Diabetic Retinopathy. Besides the capabilities above described, the system comprised a display path used for the design of internal fixation points, allowing different pupil alignments and facilitating the imaging of peripheral retinal areas. The reliability of the simulations can be directly related with BEAM IV capacity to accurately simulate actual optical components. The realism of

BEAM IV is considered high, empowered by the several variables that can be addressed to every component.

A 3D-printed mechanical prototype with a considerably ergonomic shape was designed in accordance with the objective features. The use of the rack and pinion model is intended to be a very effective way to allow the lens adjustment. The absence of the display path in this prototype is justified by the intention of testing first the fundamental optical path and only after it, implement the internal fixation points. This is possible due to the low cost of the 3D printing materials facilitating the possibility of several iterations.

Light Hazard measurements on a previously developed fundus camera prototype were performed showing that the previous prototype complied with the ISO Norms for Ophthalmic Instruments and could be regarded as a Group 2 Instrument.

The features of the prototype, coupled with its simplicity and relatively low cost (about €800, considering the external adapters for the good functioning of the optical system, excluding the smartphone) compare favourably with the products currently available, can facilitate the provision of healthcare world-wide, and make it an interesting solution for under-developed countries and isolated regions.

8.1 Future Work

After the term of the work, before the instrument can be available on the market, the improvement of some aspects is necessary. The most relevant and immediate ones are described following.

8.1.1 Optical Components Implementation

The 3D-printing of the mechanical prototype described in the chapter 5 is expected to be further developed in future work, so that the implementation of the optical system can be performed.

The prototype construction will allow the practical tests of all the features expected.

8.1.2 Light Hazard Measurements on the New Prototype

A light hazard measurement, regarding the ISO 15004-2[4] and ISO 10940[5] norms, for this kind of instruments is also mandatory, being the first for light hazard protection of Ophthalmologic Instruments and the second specifically for fundus cameras.

If the LEDs are the ones used for the measurements described in the chapter 6, the calculated values will be almost the same, as the rest of the components should have a similar transmittance for the light, don't provoking big changes in the radiation power output of the system . Even though the prototype complies with the ISO regulation for Ophthalmic devices a certification as a medical device must be obtained, by any company that takes care of the distribution of the technology.

8.1.3 Centralization of all the electronic features

Other point that is expected to be revised is the centralization of all the electronic features in a single component, as a Raspberry Pi or other small computer that provides a camera with a resolution similar to the one provided by the smartphone camera. This would improve the system by allowing both the control of the LEDs and the image acquisition in a single device.

This feature will improve the transportation as well as a probable decrease on the total cost of the fundus exam model.

Chapter 9

Publications

D. Melo, F. Soares, J. Costa, P. Vieira. (2017), "Optical Design of a Compact Image Acquisition Device for Mobile Diabetic Retinopathy Screening". Paper submitted for the conference *"BIODEVICES 2018"*, Funchal-Madeira Portugal, 19-21 January 2018. http://biodevices.biostec.org/

Bibliography

[1] *IDF Diabetes Atlas, 7th edn*. Atlas. Brussels, Belgium, 2015. URL: http://www.diabetesatlas.org.

[2] N. Cheung, P. Mitchell, and T. Y. Wong. "Diabetic retinopathy." In: *The Lancet* 376.9735 (2010), pp. 124–136. ISSN: 0140-6736. DOI: 10.1016/S0140-6736(09)62124-3. URL: http://dx.doi.org/10.1016/S0140-6736(09)62124-3.

[3] C. Bunce and R. Wormald. "Leading causes of certification for blindness and partial sight in England & Wales." In: *BMC public health* 6 (2006), p. 58. ISSN: 1471-2458. DOI: 10.1186/1471-2458-6-58.

[4] *Ophthalmic Instruments - Fundamental requirements and test methods.Part 2: Light Hazard Protection*. Standard. Geneva, CH: International Organization for Standardization, 2007.

[5] *Ophthalmic Instruments - Fundus Cameras*. Standard. Geneva, CH: International Organization for Standardization, 2009.

[6] J. M. Tarr, K. Kaul, M. Chopra, E. M. Kohner, and R. Chibber. "Pathophysiology of Diabetic Retinopathy." In: *ISRN Ophthalmology* 2013 (2013), pp. 1–13. ISSN: 2090-5696. DOI: 10.1155/2013/343560. arXiv: 343560. URL: http://www.hindawi.com/journals/isrn/2013/343560/.

[7] A. D. Deshpande, M. Harris-Hayes, and M. Schootman. "Epidemiology of Diabetes and Diabetes-Related Complications." In: *Physical Therapy* 88.11 (2008), pp. 1254–1264. DOI: 10.2522/ptj.20080020. eprint: /oup/backfile/content_public/journal/ptj/88/11/10.2522_ptj.20080020/3/ptj1254.pdf. URL: +http://dx.doi.org/10.2522/ptj.20080020.

[8] H. C. Looker, J. Krakoff, W. C. Knowler, P. H. Bennett, R. Klein, and R. L. Hanson. "Longitudinal studies of incidence and progression of diabetic retinopathy assessed by retinal photography in Pima Indians." In: *Diabetes Care* 26.2 (2003), pp. 320–326. ISSN: 01495992. DOI: 10.2337/diacare.26.2.320.

[9] M. Cignarelli, M. L. De Cicco, A. Damato, A. Paternostro, S. Pagliarini, S. Santoro, L. Cardia, G. De Pergola, and R. Giorgino. "High systolic blood pressure increases prevalence and severity of retinopathy in NIDDM patients." In: *Diabetes Care* 15.8 (1992), pp. 1002–1008. ISSN: 01495992.

[10] F. López, M. Rodríguez, J. Marticorena, and F. Gómez-Ulla. "Diabetic Retinopathy Treatment." In: *European Ophthalmic Review* 00.00 (2007), p. 68. ISSN: 1756-1795. DOI: 10.17925/EOR.2007.00.00.68. URL: http://www.touchophthalmology.com/articles/diabetic-retinopathy-treatment.

[11] J. Cunha-Vaz. "Characterization and relevance of different diabetic retinopathy phenotypes." In: *Developments in Ophthalmology* 39 (2007), pp. 13–30. ISSN: 02503751. DOI: 10.1159/000098497.

[12] T. Kauppi. *Eye Fundus Image Analysis for Automatic Detection of Diabetic Retinopathy*. 2010, p. 176. ISBN: 9789522650160.

[13] L. Giancardo. "Automated fundus images analysis techniques to screen retinal diseases in diabetic patients Docteur de l ' université Automated Fundus Images Analysis Techniques to Screen Retinal Diseases in Diabetic Patients." In: (2012).

[14] M. Gualtieri. "Avaliação funcional da visão de pacientes diabéticos em estados pré e pós retinopatia diabética." In: (2009).

[15] R. S. do Prado, E. L. Figueiredo, and T. V. B. Magalhaes. "Retinal detachment in preeclampsia." In: *Arquivos brasileiros de cardiologia* 79.2 (2002), pp. 183–186. ISSN: 0066-782X. DOI: 10.1590/S0066-782X2002001100011. URL: http://ovidsp.ovid.com/ovidweb.cgi?T=JS{\&}PAGE=reference{\&}D=med4{\&}NEWS=N{\&}AN=12219193.

[16] P. A. Sieving, R. C. Caruso, W. Tao, H. R. Coleman, D. J. S. Thompson, K. R. Fullmer, and R. A. Bush. "Ciliary neurotrophic factor (CNTF) for human retinal degeneration: phase I trial of CNTF delivered by encapsulated cell intraocular implants." In: *Proceedings of the National Academy of Sciences of the United States of America* 103.10 (2006), pp. 3896–901. ISSN: 0027-8424. DOI: 10.1073/pnas.0600236103. URL: http://www.pubmedcentral.nih.gov/articlerender.fcgi?artid=1383495{\&}tool=pmcentrez{\&}rendertype=abstract.

[17] H. Li, A. Esquivel, G. Davis, and E. Krupinski. *Evaluation of Digital Resolution for Viewing Diabetic Retinopathy Microaneurysms*. 2006.

[18] T. A. Ciulla, A. G. Amador, and B. Zinman. "Diabetic Retinopathy and Diabetic Macular Edema." In: 26.9 (2003), pp. 2653–2664.

[19] A. R.B. M. dos Santos. "Alterações Cromáticas no Edema Macular Diabético em pacientes com Diabetes Mellitus Tipo 2 : Comparação com a Espessura Retiniana." Phd Thesis. Coimbra, 2009.

[20] A. of Ophthalmology. *Diabetic Retinopathy Treatment*.

[21] "Treatment Techniques and Clinical Guidelines for Photocoagulation of Diabetic Macular Edema." In: *Ophthalmology* 94.7 (1987), pp. 761 –774. ISSN: 0161-6420. DOI: http://dx.doi.org/10.1016/S0161-6420(87)33527-4. URL: http://www.sciencedirect.com/science/article/pii/S0161642087335274.

[22] M. Q, G. MC, and W. TY. "Management of diabetic retinopathy: A systematic review." In: *JAMA* 298.8 (2007), pp. 902–916. DOI: 10.1001/jama.298.8.902. eprint: /data/journals/jama/5214/jcr70009_902_916.pdf. URL: +http://dx.doi.org/10.1001/jama.298.8.902.

[23] R. Simó and C. Hernández. "Intravitreous anti-VEGF for diabetic retinopathy: hopes and fears for a new therapeutic strategy." In: *Diabetologia* 51.9 (2008), p. 1574. ISSN: 1432-0428. DOI: 10.1007/s00125-008-0989-9. URL: https://doi.org/10.1007/s00125-008-0989-9.

[24] J. Benbassat, B. C. P. Polak, and J. C. Javitt. "Objectives of teaching direct ophthalmoscopy to medical students." In: *Acta Ophthalmologica* 90.6 (2012), pp. 503–507. ISSN: 1755375X. DOI: 10.1111/j.1755-3768.2011.02221.x.

[25] K. Tran, T. A. Mendel, K. L. Holbrook, and P. A. Yates. "Construction of an Inexpensive , Hand-Held Fundus Camera through Modification of a Consumer " Point-and-Shoot " Camera." In: 53.12 (2012), pp. 7600–7607. DOI: 10.1167/iovs.12-10449.

[26] G. Quellec, L. Bazin, G. Cazuguel, I. Delafoy, B. Cochener, and M. Lamard. "Suitability of a Low-Cost, Handheld, Nonmydriatic Retinograph for Diabetic Retinopathy Diagnosis." In: *Translational Vision Science & Technology* 5.2 (2016), p. 16. DOI: 10.1167/tvst.5.2.16. eprint: /data/journals/tvst/935082/i2164-2591-5-2-16.pdf. URL: +http://dx.doi.org/10.1167/tvst.5.2.16.

[27] K. Jin, H. Lu, Z. Su, C. Cheng, J. Ye, and D. Qian. "Telemedicine screening of retinal diseases with a handheld portable non-mydriatic fundus camera." In: *BMC Ophthalmology* 17.1 (2017), p. 89. ISSN: 1471-2415. DOI: 10.1186/s12886-017-0484-5. URL: https://doi.org/10.1186/s12886-017-0484-5.

[28] H. Schneiderman. "The Funduscopic Examination." In: *Butterworth Publishers* 2.red 2 (1990), pp. 573–580.

[29] I. Marjanovic. "The History of Detecting Glaucomatous Changes in the Optic Disc." In: *Glaucoma - Basic and Clinical Aspects*. Ed. by S. Rumelt. Rijeka: InTech, 2013. Chap. 13. DOI: 10.5772/52470. URL: http://dx.doi.org/10.5772/52470.

[30] P. De Boever, T. Louwies, E. Provost, L. Int Panis, and T. S. Nawrot. "Fundus photography as a convenient tool to study microvascular responses to cardiovascular disease risk factors in epidemiological studies." In: *Journal of visualized experiments* 92 (2014), e51904. ISSN: 1940-087X. DOI: 10.3791/51904. URL: http://www.ncbi.nlm.nih.gov/pubmed/25407823.

[31] M. A. Pérez, B. B. Bruce, N. J. Newman, and V. Biousse. "The use of retinal photography in non-ophthalmic settings and its potential for neurology." In: *Neurologist* 18.6 (2012). 23114666[pmid], pp. 350–355. ISSN: 1074-7931. DOI: 10.1097/NRL.0b013e318272f7d7. URL: http://www.ncbi.nlm.nih.gov/pmc/articles/PMC3521530/.

[32] N. Patton, T. Aslam, T. MacGillivray, A. Pattie, I. J. Deary, and B. Dhillon. "Retinal vascular image analysis as a potential screening tool for cerebrovascular disease: a rationale based on homology between cerebral and retinal microvasculatures." In: *J Anat* 206.4 (2005). 15817102[pmid], pp. 319–348. ISSN: 0021-8782. DOI: 10.1111/j.1469-7580.2005.00395.x. URL: http://www.ncbi.nlm.nih.gov/pmc/articles/PMC1571489/.

[33] B. Stanberry. "Telemedicine: Barriers and opportunities in the 21st century." In: *Journal of Internal Medicine* 247.6 (2000), pp. 615–628. ISSN: 09546820. DOI: 10.1046/j.1365-2796.2000.00699.x.

[34] B. Y. Shen and S. Mukai. "A Portable, Inexpensive, Nonmydriatic Fundus Camera Based on the Raspberry Pi® Computer." In: *Journal of Ophthalmology* 2017.3 (2017), p. 5. ISSN: 0022-2313. DOI: doi:10.1155/2017/4526243. URL: http://www.sciencedirect.com/science/article/pii/S0022231399005992.

[35] T. Swedish, K. Roesch, I. Lee, K. Rastogi, S. Bernstein, and R. Raskar. "eyeSelfie: Self Directed Eye Alignment using Reciprocal Eye Box Imaging." In: *ACM Trans. Graph.* 34.4 (2015).

[36] D-EYE S.r.l. *D-EYE Ophthalmoscope*. URL: https://www.d-eyecare.com/#vision.

[37] Volk Optical Inc. *Volk Pictor Plus*. https://volk.com/index.php/volk-products/ophthalmic-cameras/volk-pictor-plus-digital-ophthalmic-imager.html.

[38] Volk Optical Inc. *Volk Inview*. https://volk.com/index.php/volk-products/ophthalmic-cameras/volk-inview.html.

[39] A. S. Glassner, ed. *An Introduction to Ray Tracing*. London, UK, UK: Academic Press Ltd., 1989. ISBN: 0-12-286160-4.

[40] M.-C. Ho, C.-M. Chiang, P.-C. Chou, K.-F. Chang, and C.-Y. Lee. "Optimal sun-shading design for enhanced daylight illumination of subtropical classrooms." English. In: *Energy Buildings* 40.10 (2008), pp. 1844–1855. DOI: 10.1016/j.enbuild.2008.04.012.

[41] F. Jenkins and H. White. *Fundamentals of optics*. McGraw-Hill, 1957. URL: https://books.google.pt/books?id=SAwJAQAAIAAJ.

[42] L. N. Thibos, M. Ye, X. Zhang, and A. Bradley. "The chromatic eye: a new reduced-eye model of ocular chromatic aberration in humans." In: *Appl. Opt.* 31.19 (1992), pp. 3594–3600. DOI: 10.1364/AO.31.003594. URL: http://ao.osa.org/abstract.cfm?URI=ao-31-19-3594.

[43] M. Mansuripur. *Classical optics and its applications, second edition*. Cambridge University Press, Jan. 2009. ISBN: 9780511803796. DOI: 10.1017/CBO9780511803796.

[44] D. Atchison and G. Smith. "Optics of the Human Eye." In: *Butterworth-Heinemann* (2000), p. 259. DOI: 10.1016/B978-0-7506-3775-6.50001-8.

[45] M. Tocci. *How to Model the Human Eye in ZEMAX*. 2007. URL: http://www.zemax.com/kb/articles/186/1/How-to-Model-the-Human-Eye-in-ZEMAX/Page1.html.

[46] S. Sawa. *Eye fundus camera*. US Patent 4,266,861. 1981. URL: https://www.google.com/patents/US4266861.

[47] J. C. He, P. Sun, R. Held, F. Thorn, X. Sun, and J. E. Gwiazda. "Wavefront aberrations in eyes of emmetropic and moderately myopic school children and young adults." In: *Vision Research* 42.8 (2002), pp. 1063 –1070. ISSN: 0042-6989. DOI: http://dx.doi.org/10.1016/S0042-6989(02)00035-4. URL: http://www.sciencedirect.com/science/article/pii/S0042698902000354.

[48] L. Thaler, A. Schütz, M. Goodale, and K. Gegenfurtner. "What is the best fixation target? The effect of target shape on stability of fixational eye movements." In: *Vision Research* 76 (2013), pp. 31 –42. ISSN: 0042-6989. DOI: http://dx.doi.org/10.1016/j.visres.2012.10.012. URL: http://www.sciencedirect.com/science/article/pii/S0042698912003380.

[49] Canon. *Canon CR-2 PLUS AF Digital Non-Mydriatic Retinal Camera*. https://www.usa.canon.com/internet/portal/us/home/support/details/eyecare/digital-non-mydriatic-retinal-cameras/cr-2-plus-af?tab=manuals.

[50] D. Cushing. *Broad band nonreflective neutral density filter*. US Patent 4,960,310. 1990. URL: https://www.google.com/patents/US4960310.

[51] Y. P. Varshni. "Temperature dependence of the energy gap in semiconductors." In: *Physica* 34 (1967), pp. 149–154. DOI: 10.1016/0031-8914(67)90062-6.

[52] M. B. Panish and H. C. Casey. "Temperature Dependence of the Energy Gap in GaAs and GaP." In: 163.1969 (2008). DOI: 10.1063/1.1657024.

[53] M. Dyble, N. Narendran, A. Bierman, T. Klein, M. Dyble, N. Narendran, A. Bierman, and T. Klein. "Impact of Dimming White LEDs : Chromaticity Shifts Due to Different Dimming Methods." In: (2005).

[54] A. Roorda and J. L. Duncan. "Adaptive optics ophthalmoscopy." In: *Annu Rev Vis Sci* 1 (2015). 26973867[pmid], pp. 19–50. ISSN: 2374-4642. DOI: 10.1146/annurev-vision-082114-035357. URL: http://www.ncbi.nlm.nih.gov/pmc/articles/PMC4786023/.

[55] M. Born and E. Wolf. *Principles of Optics (7th Ed)*. Cambridge University Press, 1999.

[56] F. C. Delori, R. H. Webb, and D. H. Sliney. "Maximum permissible exposures for ocular safety (ANSI 2000), with emphasis on ophthalmic devices." In: *J. Opt. Soc. Am. A* 24.5 (2007), pp. 1250–1265. DOI: 10.1364/JOSAA.24.001250. URL: http://josaa.osa.org/abstract.cfm?URI=josaa-24-5-1250.

ANNEX I

Thin Lens

To reach an optimal optical system several lenses types were tested. To modulate them, according to the characteristics supplied by the manufacturers, the thin lens approximation was used. This approximation neglects the thickness of the lens and considers that the unit planes pass through the axial point of the infinitely thin lens. So it is possible to say that the rays passing through the center of the lens suffer no deviation [55]. Considering that the media on both sides of the lens is the same the following equation can be used to describe it.

Lens-Maker's Formula

$$P_{lens} = \frac{n_{lens} - n_0}{n_0}\left(\frac{1}{R_1} - \frac{1}{R_2}\right) \tag{I.1}$$

Where n_0 is the refractive index of the surrounding medium, the air in this case, equal to 1, n_{lens} is the refractive index of the lens, R_1 is the radius of curvature of the first surface and R_2 is the radius of curvature of the second surface. The P_{lens} is the refractive power in diopters. The refractive power is the reciprocal of the focal length (in meters). As the focal length is usually described in millimeters, the equation for the conversion between focal length and refractive power can be described as following.

$$P_{lens} = \frac{1000}{f} \tag{I.2}$$

Where f is the focal length in millimeters and P_{lens} is the refractive power of the lens in diopters.

These formulas are really helpful for simple lenses when the manufacturer only supplies information on the dioptric power or focal length of the lens and not on the radius of curvature. The reciprocal of the values of R_1 and R_2 are placed in the variable Curv in BEAM IV Optics Tables to describe the radius of curvature and the n_{lens} values are the ones to use in the column index.

ANNEX II

Field of View calculation

To calculate the Field of View some equations must be used. The α is half of the total Field of View in degrees (Figure II.1).

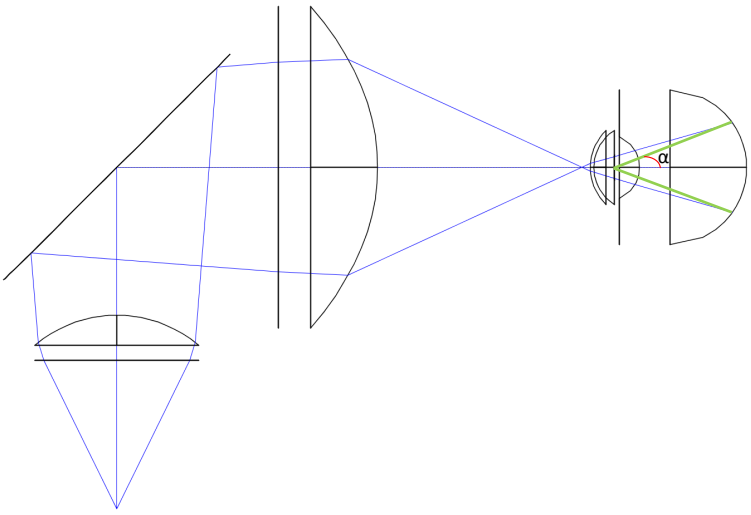

Figure II.1: Diagram showing the angle α, half of the field of view in degrees.

It is easily understandable that, having the travelled distance by the rays along the x-axis and the distance travelled along the z-axis, after passing the pupil and right before reaching the retina, the angle α will be given by the equation II.1 [56].

$$\alpha = \tan^{-1}\left(\frac{X_{distance}}{Z_{distance}}\right) \tag{II.1}$$

Where $X_{distance}$ is the distance between the extreme point in the retina and the center of the pupil in the x-axis and the $Z_{distance}$ is the central distance between the retina and the pupil in the z-axis.

Using the output of the ray tables supplied by the BEAM IV, the variables needed are the X_f and Z_f only for the rays final position. The pupil position is described in advance in the optic table. So from the equation II.1 is derived the equation II.2.

$$\alpha = \tan^{-1}\left(\frac{X_f - X_{pupil}}{Z_f - Z_{pupil}}\right) \tag{II.2}$$

As an example for the tables given in the figures II.2 and II.3 the Field of the View calculation is as following :

$$\begin{aligned} &\alpha = \tan^{-1}\left(\frac{6.94 - 0}{165.39 - 147}\right); \\ &\alpha = tan^{-1}(0.377); \\ &\alpha = 20.66°. \end{aligned} \tag{II.3}$$

To get the Field of View it is only needed to multiply α for two.

$$\begin{aligned} &FOV = 2 \times \alpha; \\ &FOV = 2 \times 20.66°; \\ &FOV = 41.32°. \end{aligned} \tag{II.4}$$

8 rays PCXrodado.RAY

Z0		X0		U0		W0	V0		Zf	Xf
70	:	-53	A	1	:	0.490000X	0	:	165.389889:	-6.9398:
70	:	-53	A	1	:	-0.490000X	0	:	165.389889:	6.9398:
70	:	-53	A	1	:	:	0.49000	:	165.389889:	-0.0000:
70	:	-53	A	1	:	:	-0.490	:	165.389889:	-0.0000:

Figure II.2: Ray table showing the final position of the rays (X_f and Z_f variables).

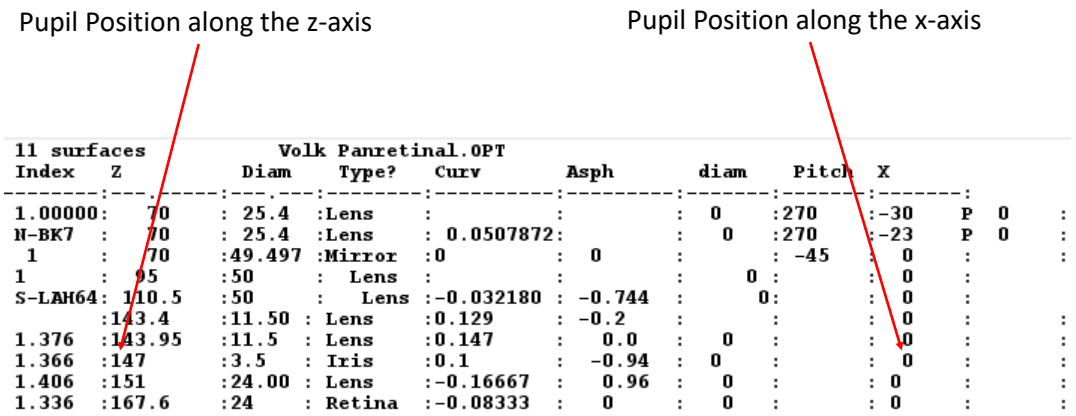

Figure II.3: Optics table where the position of the pupil can be assessed.

ANNEX III

Pulse Width Modulation

The PWM is one of the most important ways to control the luminosity of a LED. It considers that the intensity is controlled by the Duty Cycle [53]. This means that only by switching the system on and off at an high frequency rate, making it imperceptible for the observer, it is possible to control the intensity of light emitted by the LED .

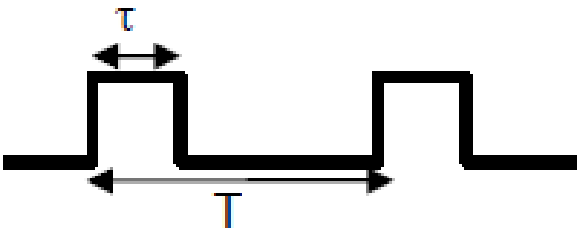

Figure III.1: Pulse Width Modulation demonstration. The system is switched on and off. When each pulse occurs, the signal is sent to the LED. The variables τ and T are, respectively, the pulse width and the period between pulses.[53]

From the variables presented in the figure III.1 the Duty Cycle is obtained by the equation III.1.

$$D = \frac{\tau}{T} \tag{III.1}$$

Where D is the Duty Cycle, τ is the pulse width and T is the period. Knowing the Duty Cycle the Average Current is easily calculated by the equation III.2.

$$I_{Average} = I_{Peak} \times D \tag{III.2}$$

The changes in the $I_{Average}$ is what will produce alterations in the LED intensity. When one changes the intensity of light in the smartphone application described in the chapter 6 is actually changing the average intensity of the current.

ANNEX IV

Spectrum and Power Measurements Setups

Three different setups were needed to calculate the emission spectrum and the power emitted by each LED as well as the voltage and time lapse for the Acquisition Mode.

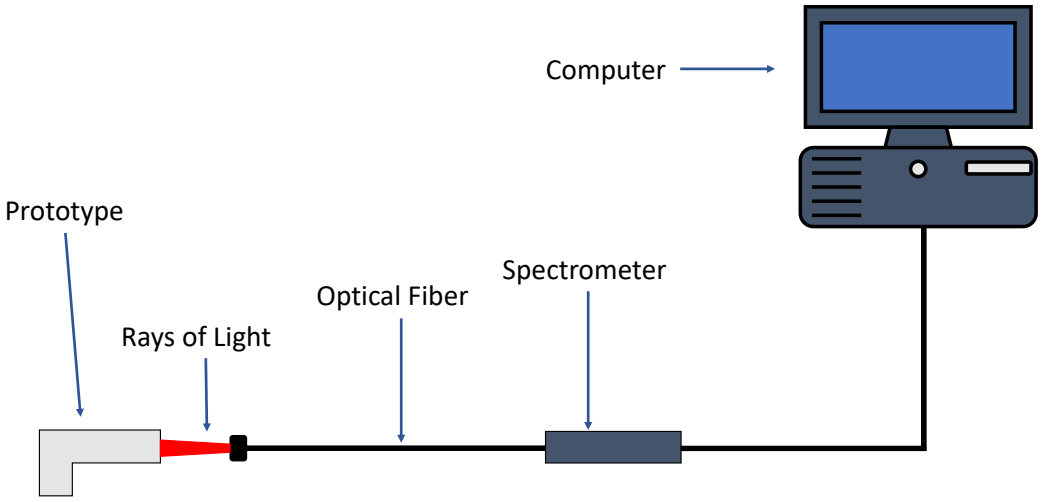

Figure IV.1: Scheme representing the setup for acquisition of the spectrums. The optical fiber is placed in the focal distance of the system so all the rays are collected. A neutral density optical filter was needed to prevent the saturation of the spectrometer.

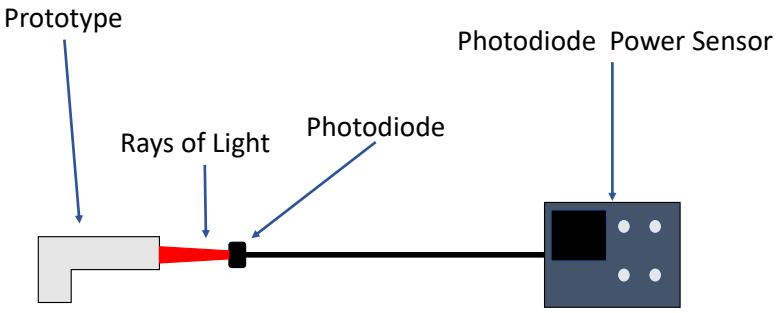

Figure IV.2: Scheme representing the setup for power measurement. The photodiode is placed in the focal distance of the system so all the rays are collected and the photodiode power sensor measured the power at specific wavelengths.

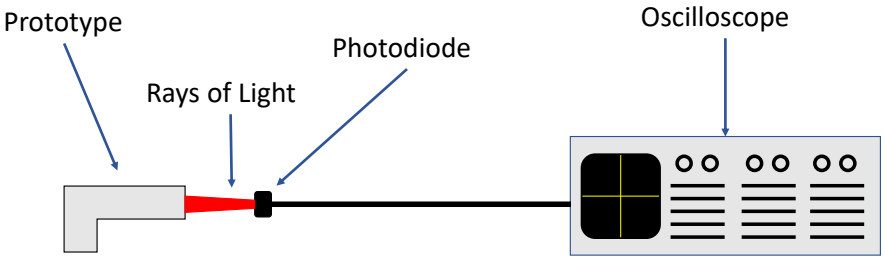

Figure IV.3: Scheme representing the setup for the voltage measurement on the Acquisition Mode. The photodiode is placed in the focal distance of the system so all the rays are collected and the Oscilloscope demonstrates the voltage change caused by the Flash.

ANNEX V

Spectrometer Output Text File

```
Integration time [ms]:  63.216
Averaging Nr. [scans]: 8
Smoothing Nr. [pixels]: 0
Data measured with spectrometer [name]: 0606012U1
Wave     Sample     Dark       Reference Scope
[nm]     [counts]   [counts]   [counts]

 323.80   863.000  1124.000   487.520
 324.40   873.000  1208.000   487.040
 324.99   831.000  1060.000   484.280
 325.59   839.500  1000.000   495.000
 326.18   857.500  1132.000   488.120
 326.78   867.500  1072.000   487.200
 327.38   865.000  1096.000   483.040
 327.97   884.500  1160.000   483.120
 328.57   892.500  1240.000   489.400
 329.16   913.000  1312.000   488.960
 329.76   859.000   952.000   485.360
 330.36   809.500   856.000   479.280
 330.95   818.000   928.000   478.640
 331.55   813.500   932.000   484.480
 332.14   840.000  1044.000   482.360
 332.74   876.500  1192.000   488.680
 333.33   816.500   968.000   481.760
 333.93   880.000  1140.000   486.400
 334.52   845.500   988.000   476.520
 335.12   862.000   960.000   488.120
 335.72   866.000  1116.000   495.400
 336.31   873.000   956.000   482.640
 336.91   951.500  1516.000   495.440
 337.50   842.500   964.000   482.720
 338.10   849.000   976.000   480.920
 338.69   802.000   896.000   482.640
 339.29   865.000  1036.000   488.920
 339.88   820.000   992.000   490.320
 340.48   896.500  1344.000   492.160
 341.07   879.000  1088.000   490.600
 341.67   876.500  1216.000   486.640
 342.26   836.500  1124.000   479.880
 342.86   846.000  1016.000   482.720
 343.45   820.000   876.000   482.320
 344.05   869.000  1044.000   488.880
 344.64   852.500  1000.000   486.680
```

Figure V.1: Demonstration of the spectrometer output text file.

ANNEX VI

Code used for the spectrum analysis

In this annex will be presented the code used for processing the files containing the spectrums obtained with the AvaSoft software (example in the annex V). The output obtained with the Avasoft is in the form of text file containing the number of counts at each wavelength . To extract the values of the needed variables the following code is used since the LED only has one peak.

```
import matplotlib.pyplot as plt
import sys
import numpy as np
from scipy.special import erf
from scipy.optimize import curve_fit
```

The following functions define the gaussian fit curve , having the initial spectrum. For the NIR spectrum only the asym_peak function is used as it only has one peak.

```
def asym_peak(x,*pars): # approximation for one peak spectrum
    z = np.zeros_like(x)
    ctr = pars[0]  # wavelength
    amp = pars[1]  # amplitude
    wid = pars[2]  # width of gaussian
    z = z + amp * np.exp(-((x - ctr) / wid) ** 2)
    return z
```

```
def two_peaks(t, *pars):  # approximation for two peaks spectrum
    ctr1 = pars[0]  # wavelength
    amp1 = pars[1]  # amplitude
    wid1 = pars[2]  # width of gaussian
    ctr2 = pars[3]   # wavelength
    amp2 = pars[4]  # amplitude
    wid2 = pars[5]  # width of gaussian
    parguess1=(ctr1, amp1, wid1)
    parguess2 = (ctr2, amp2, wid2)
    p1 = asym_peak(t,*parguess1 )
    p2 = asym_peak(t, *parguess2)
    return p1 + p2
```

The following code for spectrum processing is separated according to the type of light. First each NIR spectrum is obtained and the area beneath the peak is calculated by usage of the Gaussian Fit. Then the same occurs for the visible spectrum, but instead of using the Gaussian fit for one peak, is used the two_peaks function having in account both peaks.

```
orig_stdout = sys.stdout # write the output text file
s = open('Spectrum(1).txt', 'w')
sys.stdout = s


f = 'NIR5.TXT'
g = 'NIR15.TXT'
h = 'NIR30.TXT'
l = 'NIR255.TXT'
list = [f, g, h, l]
for a in list: #opening of the text files of the NIR spectrum
    x = open(a, 'r')
    header1 = x.readline()
    header2 = x.readline()
    header3 = x.readline()
    header4 = x.readline()
    header5 = x.readline()
    header6 = x.readline()
```

```
header7 = x.readline()
header8 = x.readline()
wlraw = []  #initialization of the lists
intensityraw = []
i = 0
for line in x: #read each line of the text file
    line = line.strip()
    columns = line.split()
    wl = float(columns[0])  #storage of the wavelength
    intensity = float(columns[1])  #storage of the counts
    wlraw.append(wl)
    intensityraw.append(intensity)
    i = (i + 1)
wlraw = np.array(wlraw)
intensityraw = np.array(intensityraw)
intensityraw -= np.mean(intensityraw[(wlraw > 400) & (wlraw < 700)]) #normalization
maximum_indices = np.where(intensityraw == (max(intensityraw)))
headerline = header2.strip()
headercolumns = headerline.split()  #extraction of the integration time
integrationtime = float(headercolumns[3])
if (a == f):   #processment for each smartphone level
    print("")
    print("Near Infra-Red 5")
    print("")
    fig1 = plt.figure()
    ax1 = fig1.add_subplot(111)
    ax5 = fig1.add_subplot(111)
    parguess = (820, 50000, 55)  #One peak guess
    fig1.suptitle('Near Infra-Red 5')
    plt.xlabel('Wavelength(nm)')
    plt.ylabel('Intensity')
    plt.plot(wlraw, intensityraw,'b-')  #Plot of the spectrum
    popt, pcov = curve_fit(asym_peak, wlraw, intensityraw, parguess)   #Gaussian fit
    plt.plot(wlraw, asym_peak(wlraw, *popt), 'r-') #Plot of the Gaussina fit
    plt.legend(['spectrum',   'gaussian fit'])
    fig1.savefig('Near Infra-Red 5 Spectrum(1).jpg')
if (a == g):
    print("")
    print("Near Infra-Red 15")
    print("")
    fig2 = plt.figure()
```

```
        ax2 = fig2.add_subplot(111)
        ax6 = fig1.add_subplot(111)
        parguess = (820, 50000, 55)
        fig2.suptitle('Near Infra-Red 15')
        plt.xlabel('Wavelength(nm)')
        plt.ylabel('Intensity')
        plt.plot(wlraw, intensityraw,'b-')
        popt, pcov = curve_fit(asym_peak, wlraw, intensityraw, parguess)
        plt.plot(wlraw, asym_peak(wlraw, *popt), 'r-')
        plt.legend(['spectrum',   'gaussian fit'])
        fig2.savefig('Near Infra-Red 15 Spectrum(1).jpg')
    if (a == h):
        print("")
        print("Near Infra-Red 30")
        print("")
        fig3 = plt.figure()
        ax3 = fig3.add_subplot(111)
        ax6 = fig1.add_subplot(111)
        parguess = (820, 50000, 55)
        fig3.suptitle('Near Infra-Red 30')
        plt.xlabel('Wavelength(nm)')
        plt.ylabel('Intensity')
        plt.plot(wlraw, intensityraw,'b-')
        popt, pcov = curve_fit(asym_peak, wlraw, intensityraw, parguess)
        plt.plot(wlraw, asym_peak(wlraw, *popt), 'r-')
        plt.legend(['spectrum',   'gaussian fit'])
        fig3.savefig('Near Infra-Red 30 Spectrum(1).jpg')
    if (a == l):
        print("")
        print("Near Infra-Red 255")
        print("")
        fig4 = plt.figure()
        ax4 = fig4.add_subplot(111)
        ax8 = fig1.add_subplot(111)
        parguess = (820, 50000, 55)
        fig4.suptitle('Near Infra-Red 255')
        plt.xlabel('Wavelength(nm)')
        plt.ylabel('Intensity')
        plt.plot(wlraw, intensityraw,'b-')
        popt, pcov = curve_fit(asym_peak, wlraw, intensityraw, parguess)
        plt.plot(wlraw, asym_peak(wlraw, *popt), 'r-')
```

```
        plt.legend(['spectrum',   'gaussian fit'])
        fig4.savefig('Near Infra-Red 255 Spectrum(1).jpg')
    pars1 = popt[0:3] #Variables from the gaussian fit
    peak1 = asym_peak(wlraw, *pars1)
    area1 = np.trapz(peak1, wlraw)

    print("Integration Time = ", integrationtime, "s")
    print("Peak = ", float(wlraw[maximum_indices]),"nm")
    print("Area = ", area1)
    print("Area divided by the integration time=", area1/integrationtime)

    x.close()

f = 'VISI5.TXT'
g = 'VISI30.TXT'
h = 'VISI100.TXT'
l = 'VISI255.TXT'
list = [f,g,h,l]
for a in list: #opening text files of the Visible spectrum
    x=open(a,'r')
    header1 = x.readline()
    header2 = x.readline()
    header3 = x.readline()
    header4 = x.readline()
    header5 = x.readline()
    header6 = x.readline()
    header7 = x.readline()
    header8 = x.readline()
    wlraw = []  #initialization
    intensityraw = []
    i = 0
    for line in x:#read each line of the text file
        line = line.strip()
        columns = line.split()
        wl = float(columns[0])
        intensity = float(columns[1])
        wlraw.append(wl)               #storage of the wavelength
        intensityraw.append(intensity) #storage of the counts
        i = (i + 1)
    wlraw=np.array(wlraw)
    intensityraw=np.array(intensityraw)
```

```
intensityraw -= np.mean(intensityraw[(wlraw > 800) & (wlraw< 1050)]) #normalization
headerline = header2.strip()
headercolumns = headerline.split()
integrationtime = float(headercolumns[3]) #extraction of the integration time
if (a == f):#processment for each smartphone level
    print("")
    print("Visible 5")
    print("")
    fig5 = plt.figure()
    ax9 = fig5.add_subplot(111)
    fig5.suptitle('Visible 5')
    plt.xlabel('Wavelength(nm)')
    plt.ylabel('Intensity')
    parguess = (450, 50000, 40, 570 ,40000,30) #Two peaks guess
    popt, pcov = curve_fit(two_peaks, wlraw, intensityraw, parguess) #Gaussian fit
    plt.plot(wlraw, intensityraw,'b-') #Plot of the spectrum
    plt.plot(wlraw, two_peaks(wlraw, *popt), 'r-') #Plot of the Gaussian Fit
    plt.legend(['spectrum',   'gaussian fit'])
    fig5.savefig('Visible 5 Spectrum.jpg')
if (a == g):
    print("")
    print("Visible 30")
    print("")
    fig6 = plt.figure()
    ax6 = fig6.add_subplot(111)
    ax10 = fig5.add_subplot(111)
    fig6.suptitle('Visible 30')
    plt.xlabel('Wavelength(nm)')
    plt.ylabel('Intensity')
    parguess = (450, 55000, 55, 570 ,25000,30)
    popt, pcov = curve_fit(two_peaks, wlraw, intensityraw, parguess)
    plt.plot(wlraw, intensityraw,'b-')
    plt.plot(wlraw, two_peaks(wlraw, *popt), 'r-')
    plt.legend(['spectrum',   'gaussian fit'])
    fig6.savefig('Visible 30 Spectrum.jpg')
if (a == h):
    print("")
    print("Visible 100")
    print("")
    fig7 = plt.figure()
    ax11 = fig5.add_subplot(111)
```

```
        fig7.suptitle('Visible 100')
        plt.xlabel('Wavelength(nm)')
        plt.ylabel('Intensity')
        parguess = (450, 55000, 55, 570 ,15000,30)
        popt, pcov = curve_fit(two_peaks, wlraw, intensityraw, parguess)
        plt.plot(wlraw, intensityraw,'b-')
        plt.plot(wlraw, two_peaks(wlraw, *popt), 'r-')
        plt.legend(['spectrum',   'gaussian fit'])
        fig7.savefig('Visible 100 Spectrum.jpg')
    if (a == 1):
        print("")
        print("Visible 255")
        print("")
        fig8 = plt.figure()
        ax12 = fig5.add_subplot(111)
        fig8.suptitle('Visible 255')
        plt.xlabel('Wavelength(nm)')
        plt.ylabel('Intensity')
        parguess = (450, 55000, 55, 570 ,5000,30)
        popt, pcov = curve_fit(two_peaks, wlraw, intensityraw, parguess)
        plt.plot(wlraw, intensityraw,'b-')
        plt.plot(wlraw, two_peaks(wlraw, *popt), 'r-')
        plt.legend(['spectrum',   'gaussian fit'])
        fig8.savefig('Visible 255 Spectrum.jpg')
    pars1 = popt[0:3] #Variables from the gaussian fit for the first peak
    pars2 = popt[3:6] #Variables from the gaussian fit for the second peak

    peak1 = asym_peak(wlraw, *pars1)
    peak2 = asym_peak(wlraw, *pars2)

    area1 = np.trapz(peak1, wlraw)
    area2 = np.trapz(peak2, wlraw)
    print("Integration Time = ", integrationtime, "s")
    print("Blue peak = " ,popt[0], "nm" )
    print("Blue area=", area1)
    print("Blue area with divided by the integration time = ", area1/integrationtime)
    print("Blue maximum counts=", popt[1])
    print("Yellow Peak = ", popt[3],"nm")
    print("Yellow Area=", area2)
    print("Yellow area divided by the integration time = ", area2/integrationtime)
    print("Yellow Maximum Counts=", popt[4])
```

```
        print('Blue area is {0:1.2%} of the total area'.format(area1 / (area1 + area2)))
        print('Yellow area is {0:1.2%} of the total area'.format(area2 / (area1 + area2)))
        x.close()
plt.show()
sys.stdout = orig_stdout
s.close()
```

ANNEX VII

LED Spectrums

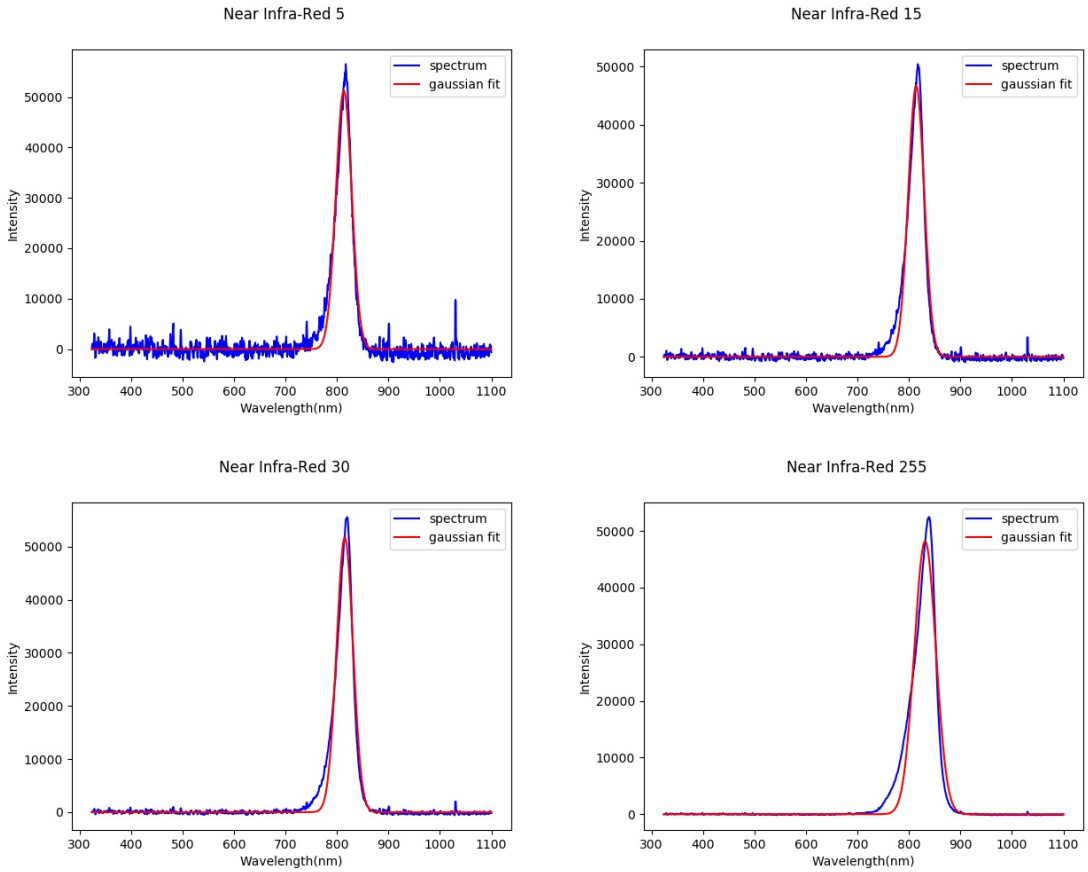

Figure VII.1: NIR LED Spectrums for each of the smartphone levels. The spectrums are presented in blue and in red the approximation with the Gaussian Fit Curve.

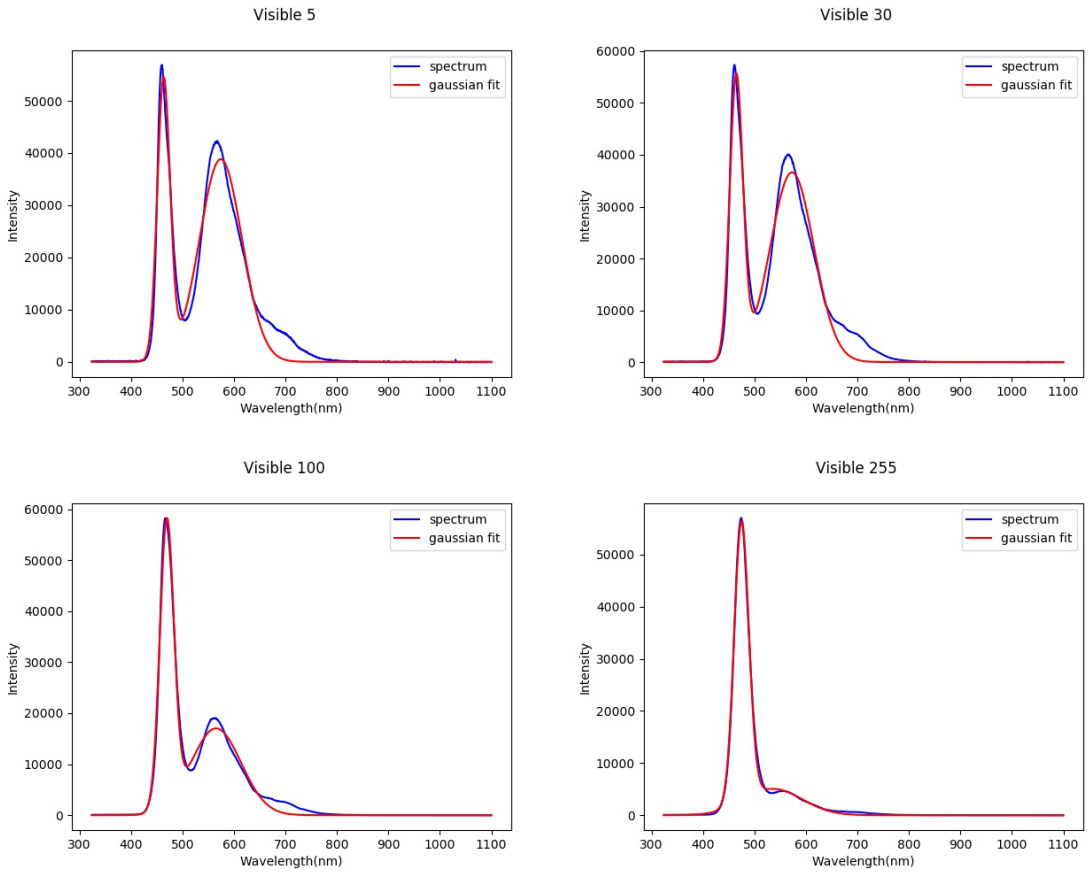

Figure VII.2: Visible LED Spectrums for each of the smartphone levels. The spectrums are presented in blue and in red the approximation with the Gaussian Fit Curve.

ANNEX VIII

Output Text File

Near Infra-Red 5

Integration Time = 3768.155 s
Peak = 816.94 nm
Area = 1985357.93488
Area divided by the integration time= 526.877990655

Near Infra-Red 15

Integration Time = 1300.0 s
Peak = 816.94 nm
Area = 1819484.25935
Area divided by the integration time= 1399.60327642

Near Infra-Red 30

Integration Time = 789.714 s
Peak = 819.75 nm
Area = 2074194.45733
Area divided by the integration time= 2626.51346858

Near Infra-Red 255

Integration Time = 186.322 s
Peak = 839.39 nm

Area = 2526265.03393
Area divided by the integration time= 13558.5976639

Visible 5

Integration Time = 63.216 s
Blue peak = 463.298582804 nm
Blue area= 1664250.09726
Blue area with divided by the integration time = 26326.4062463
Blue maximum counts= 53488.6243918
Yellow Peak = 574.215188053 nm
Yellow Area= 4020837.07755
Yellow area divided by the integration time = 63604.7373695
Yellow Maximum Counts= 38827.6924428
Blue area is 29.27% of the total area
Yellow area is 70.73% of the total area

Visible 30

Integration Time = 17.159 s
Blue peak = 464.502416948 nm
Blue area= 1741436.21581
Blue area with divided by the integration time = 101488.21119
Blue maximum counts= 54292.1956508
Yellow Peak = 572.805597247 nm
Yellow Area= 3910527.032
Yellow area divided by the integration time = 227899.471531
Yellow Maximum Counts= 36622.2833502
Blue area is 30.81% of the total area
Yellow area is 69.19% of the total area

Visible 100

Integration Time = 6.619 s
Blue peak = 469.430253949 nm
Blue area= 1908099.20623
Blue area with divided by the integration time = 288276.054726
Blue maximum counts= 55848.521842
Yellow Peak = 565.017656007 nm
Yellow Area= 2067007.06591
Yellow area divided by the integration time = 312283.889698

Yellow Maximum Counts= 17013.6738378
Blue area is 48.00% of the total area
Yellow area is 52.00% of the total area

Visible 255

Integration Time = 3.041 s
Blue peak = 474.588878134 nm
Blue area= 1909258.28241
Blue area with divided by the integration time = 627838.961659
Blue maximum counts= 53599.8043489
Yellow Peak = 536.369298647 nm
Yellow Area= 714088.86767
Yellow area divided by the integration time = 234820.410283
Yellow Maximum Counts= 5040.58031511
Blue area is 72.78% of the total area
Yellow area is 27.22% of the total area